Along-Trench Structural Variations of the Subducting Juan de Fuca Plate From Multichannel Seismic Reflection Imaging

Shuoshuo Han, Suzanne M. Carbotte, Juan Pablo Canales, Mladen R. Nedimović, Hélène Carton

AGU100 ADVANCING EARTH AND SPACE SCIENCE

JGR

Journal of Geophysical Research: Solid Earth

RESEARCH ARTICLE

10.1002/2017JB015059

Key Points:
- We find more extensive faulting deformation in the Juan de Fuca Plate near the deformation front south of 45.8°N compared with the north
- Propagator wakes are structural and hydration heterogeneities in the subducting JdF Plate and may contribute to Cascadia ETS segmentation
- Four WNW trending strike-slip faults that cross the Cascadia deformation front are imaged that transect the crust of the incoming JdF Plate

Supporting Information:
- Supporting Information S1
- Figure S2

Correspondence to:
S. Han,
han@ig.utexas.edu

Citation:
Han, S., Carbotte, S. M., Canales, J. P., Nedimović, M. R., & Carton, H. (2018). Along-trench structural variations of the subducting Juan de Fuca Plate from multichannel seismic reflection imaging. *Journal of Geophysical Research: Solid Earth*, *123*, 3122–3146. https://doi.org/10.1002/2017JB015059

Received 2 OCT 2017
Accepted 22 MAR 2018
Accepted article online 30 MAR 2018
Published online 22 APR 2018

Along-Trench Structural Variations of the Subducting Juan de Fuca Plate From Multichannel Seismic Reflection Imaging

Shuoshuo Han[1,2,3], Suzanne M. Carbotte[1], Juan Pablo Canales[4], Mladen R. Nedimović[1,5], and Hélène Carton[1,6]

[1]Lamont-Doherty Earth Observatory, Palisades, NY, USA, [2]Department of Earth and Environmental Sciences, Columbia University, New York, NY, USA, [3]Now at Institute for Geophysics, University of Texas at Austin, Austin, TX, USA, [4]Woods Hole Oceanographic Institution, Woods Hole, MA, USA, [5]Department of Earth Sciences, Dalhousie University, Halifax, Nova Scotia, Canada, [6]Institut de Physique du Globe de Paris, Paris, France

Abstract To characterize the along-strike structural variations of the Juan de Fuca (JdF) Plate as it enters the Cascadia subduction zone, we present prestack time migrated multichannel seismic reflection images of the JdF Plate along a 400-km-long trench-parallel transect extending from 44.3°N to 47.8°N. Beneath the 1.8–3.0-km-thick sediment cover, our data reveal basement topographic anomalies associated with a 1.2-km-high seamount and in the vicinity of propagator wakes (390–540-m relief). Weak Moho reflections are imaged beneath the propagator wakes and coincide with reduced Vp in the lower crust and/or uppermost mantle. The inferred locations of propagator wakes in the downgoing plate collocate with some of the boundaries of episodic tremor and slip events. We propose that the structural and hydration heterogeneities associated with these features could lead to anomalous plate interface properties and contribute to episodic tremor and slip segmentation. Intracrustal reflections with apparent dips (20°–30°) consistent with subduction bending normal faults change near 45.8°N, from northward dipping reflections confined to the middle crust in the north to antithetic reflections through the crust in the south, coinciding with a Vp reduction in the lower crust. These observations indicate more extensive faulting deformation and associated hydration of the JdF Plate south of 45.8°N, which likely results from variations of slab dip and resistance to subduction across 46°N. Basement offsets and abrupt depth/amplitude changes in Moho reflections are imaged beneath the four major WNW trending strike-slip faults that cross the Cascadia deformation front, providing strong evidence of a lower plate origin for these faults.

1. Introduction

The Cascadia subduction zone exhibits along-strike variations in a number of subduction processes. While instrumentally recorded seismicity from plate interface is exceedingly low for much of the margin (Morton & Bilek, 2015; Obana et al., 2015; Stone et al., 2018; Tréhu et al., 2015, 2008), paleoseismic studies reveal repeated great megathrust earthquakes during the Holocene (Atwater, 1987; Atwater & Hemphill-Haley, 1997; Goldfinger et al., 2003), with hypothesized recurrence intervals from ~220 years in the south to 480–505 years in the north (Goldfinger et al., 2017). Gravity anomalies and coastal subsidence data suggest heterogeneous coseismic slip during megathrust earthquakes along the margin, with low slip regions near Netarts Bay (~45.4°N), Alsea Bay (~44.4°N), and Cape Blanco (~42.5°N; P. Wang et al., 2013; Wells et al., 2003). Land-based geodetic data reveal reduced interseismic uplift in Central Cascadia between 43°N and 46°N in comparison to further north and south, suggesting possibly weaker megathrust coupling in this region (Burgette et al., 2009; McCaffrey et al., 2013; Schmalzle et al., 2014). Downdip of the seismogenic zone (25–45-km depth), episodic tremor and slip (ETS) events are segmented along the margin, with different recurrence intervals of 10 to 19 months for the different segments (Boyarko et al., 2015; Brudzinski & Allen, 2007).

Although numerous factors such as dynamic rupture processes or stage within the earthquake cycle (e.g., Noda & Lapusta, 2013) may contribute to the along-strike variations in plate interface slip behavior at Cascadia, geological controls may play an important role, too. Studies to date have primarily considered the potential role of variations in the structure and properties of the overriding North American Plate. For example, creeping along the megathrust offshore central Oregon is inferred from land-based geodetic measurements and has been attributed to the low permeability of the upper plate in this region, which hinders the upward migration of fluid generated from slab dehydration and causes overpressure at the plate

interface (Schmalzle et al., 2014). Differences in ETS recurrence intervals and tremor density along the margin have been linked to the topography, composition, and fault density of the different continental terranes of the North American Plate, which may lead to differences in upper plate strength and permeability and modulate the frictional properties and pore fluid pressure on the plate interface (Audet & Bürgmann, 2014; Brudzinski & Allen, 2007; Wells et al., 2017).

In addition to upper plate properties, there is abundant evidence from other subduction zones that variations in the structure and properties of the downgoing plate can also contribute to along-strike variations in subduction processes. For instance, local topographic anomalies associated with seamounts, aseismic ridges, and fracture zones are thought to influence plate interface slip behavior (Bell et al., 2010; K. Wang & Bilek, 2011). An assessment of the history of $Mw > 7.0$ earthquakes along the Peru-Chile subduction zone since 1500 Common Era indicates that earthquake ruptures tend to stop at major bathymetric features in the downgoing plate including the Mocha and Challenger Fracture Zones and the Chile Rise (Contreras-Reyes & Carrizo, 2011). Using Global Positioning System measurements in central Chile, Métois et al. (2012) determine several narrow zones of low interseismic coupling along the Chile margin that coincide with subducting fracture zones or ridges. At the Sumatra margin, subducting ridges and seamounts appear to serve as rupture barriers in past major earthquakes (Henstock et al., 2016; Singh et al., 2011). Further downdip within the slab, the abundance of intermediate-depth intraslab earthquakes at the Middle America, central northern Chile, and Alaska subduction zones correlates well with the extent of subduction bend faulting deformation in the incoming oceanic plate (Ranero et al., 2005; Shillington et al., 2015). These faults are believed to transect the oceanic crust and facilitate hydration of the uppermost mantle, greatly increasing the amount of water entering the subduction zone and promoting the generation of intermediate-depth intraslab earthquakes through dehydration embrittlement (Kirby et al., 1996; Ranero et al., 2003, 2005).

At Cascadia a thick sediment blanket covers the Juan de Fuca (JdF) Plate and little is known of the structure and properties of the subducting plate as it enters the trench. Seamounts are observed near the JdF Ridge and are abundant on the Pacific Plate, but their distribution in the JdF Plate interior and near the deformation front is largely unknown. While major fracture zones like those subducting along the Peru-Chile margin are not found at Cascadia, magnetic anomalies reveal a series of oblique-trending propagator wakes (Wilson, 1993, 2002) that intersect the margin, which are known to be topographic and structural anomalies from prior studies in the plate interior (Calvert et al., 1990; Carbotte et al., 2008; Hasselgren & Clowes, 1995; Hasselgren et al., 1992; Marjanović et al., 2011; McClymont & Clowes, 2005; Nedimović et al., 2005). These features are heterogeneities in the downgoing plate, potentially analogous to fracture zones. Although released fluids from propagator wakes have been proposed to contribute to forearc earthquakes at Vancouver Island (McCrory et al., 2012; Nedimović et al., 2009), their impact on Cascadia subduction zone processes has not been systematically investigated till now. Near the deformation front, evidence for faulting due to subduction bending is found in legacy seismic data acquired before the mid-1990s but is primarily limited to observations of faults within the sediment section (Nedimović et al., 2009, and references therein), and thus, the extent of faulting and hydration within the crust and upper mantle prior to subduction has been largely unknown.

In 2012, the JdF Ridge-to-Trench experiment was conducted to study the evolution and state of hydration of the crust and shallow mantle of the JdF Plate prior to subduction at the Cascadia margin (Canales et al., 2017; Carbotte et al., 2012; Han et al., 2016; Horning et al., 2016). During this study multichannel seismic (MCS) and wide-angle ocean bottom seismometer (OBS) data were acquired along three transects (Figure 1). From reflection images and velocity models of two cross-plate transects (located offshore central Oregon and Washington, hereafter referred to as OR and WA transects), crustal structure, distribution and extent of faulting, and evolution of the hydration state of the plate are characterized from the JdF Ridge to Cascadia deformation front (Han et al., 2016; Horning et al., 2016). From a study of *P* wave seismic velocity structure along the trench-parallel transect (MARGIN transect), along-strike variation of JdF Plate hydration near the deformation front prior to subduction is quantified (Canales et al., 2017).

In this study, MCS data from the MARGIN transect of the JdF Ridge-to-Trench experiment are used to characterize the structure of the incoming plate just prior to subduction from 44.3° to 47.8°N, corresponding to 1/3 of the total length of the Cascadia margin. Our data provide new constraints on the seismic structure of three propagator wakes entering the subduction zone and a group of WNW trending strike-slip faults (SSFs) that

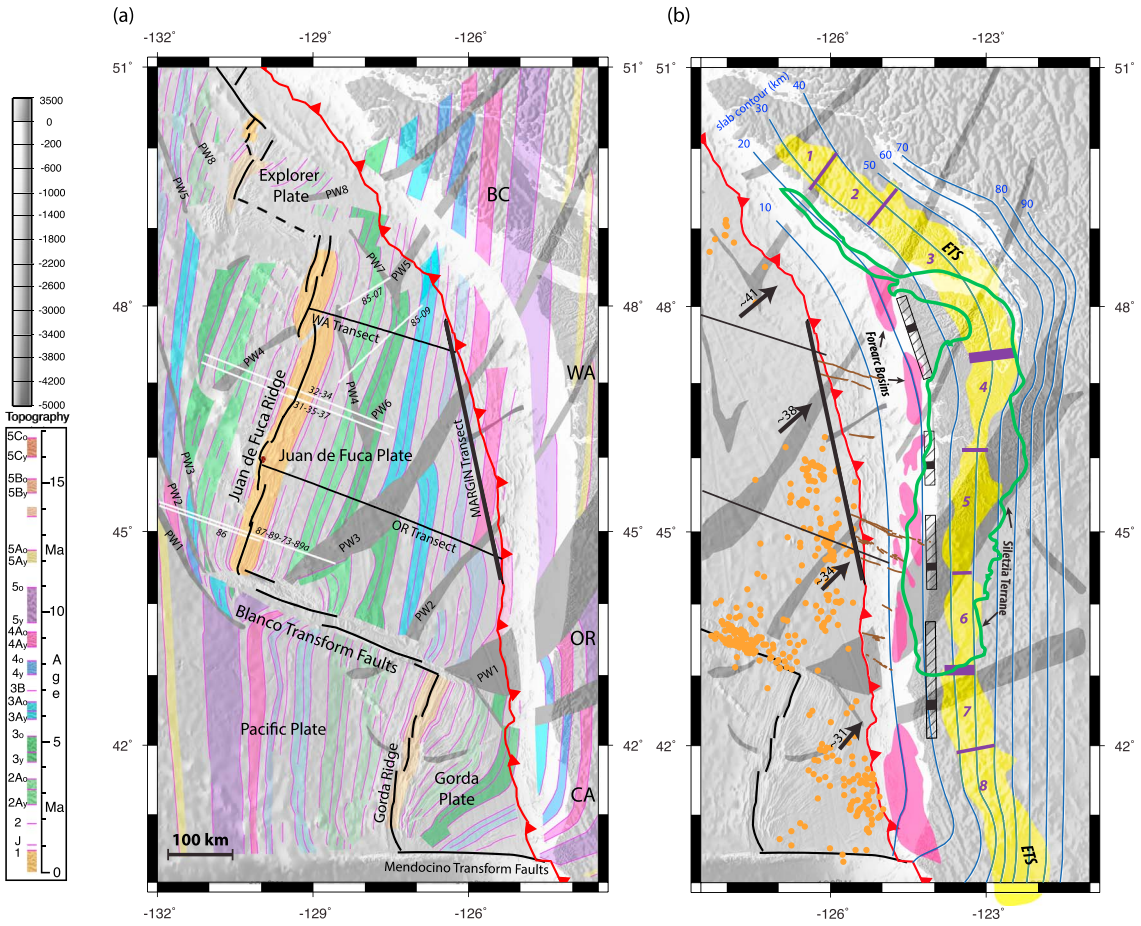

Figure 1. Regional map of the Juan de Fuca (JdF) Plate and the Cascadia subduction zone. (a) The JdF Plate: the JdF Ridge, Gorda Ridge, Blanco transform fault, and Mendocino transform fault are shown by thin black lines. The deformation front of the Cascadia subduction zone is shown by barbed red line. The MARGIN transect from the JdF Ridge-to-Trench experiment is indicated by thick black line, and the two cross-plate transects (OR and WA transects) from the same survey are shown as thin black lines. Survey lines from previous seismic experiments are in thin white lines. Crustal age from Wilson (2002) shown as colored bands is superimposed over gray scale bathymetry. Propagator pseudofault zones interpreted from offset magnetic anomalies are indicated by dark gray bands and are numbered according to their propagation episodes, following the numbering convention of Karsten and Delaney (1989). Abbreviation: BC = British Columbia; WA = Washington; OR = Oregon; CA = California; PW = propagator wake. (b) The Cascadia subduction zone: plate boundaries are the same as in (a). Brown lines near the deformation front show oblique strike-slip faults identified by Goldfinger et al. (1997). Pink shaded regions indicate forearc basins identified by Wells et al. (2003). Boundaries of paleoearthquake rupture segments estimated from offshore turbidites are shown in black rectangles with the uncertainty ranges indicated by hatched rectangles (Goldfinger et al., 2017). Yellow band shows the distribution of tremor events (8 March 2010 to 8 March 2012; obtained from A. Wech, http://www.pnsn.org/tremor). Boundaries of episodic tremor and slip (ETS) segments from Boyarko et al. (2015) are indicated by purple lines on top of the yellow band; the two bold lines show major recurrence interval boundaries at 42.8°N and 47.5°N, the other five thin lines show secondary boundaries. ETS segments are numbered. Fine blue lines show slab depth contours from McCrory et al. (2012) with contour depth indicated. The outline of the Siletz terrane is shown in thick green line (McCrory & Wilson, 2013). The convergence rates in mm/yr of the JdF Plate with respect to the North American Plate are shown in black arrows (Kreemer et al., 2014). Orange dots indicate microearthquakes in the incoming JdF Plate and the Gorda Plate detected using near-trench stations of Cascadia Initiative array (Stone et al., 2018). Catalog is considered complete within 70 km seaward of the deformation front. This figure is modified after Nedimović et al. (2009).

obliquely transect the deformation front in this region. Our reflection images also reveal abundant reflectivity in the JdF crust that is likely related to subduction bend faulting and a prominent transition in crustal reflectivity near 45.8°N. Implications of these results for the segmentation of ETS, hydration processes of the JdF Plate, and the formation mechanisms of the oblique SSFs are discussed.

2. Geological Background

At the Cascadia subduction zone, the 6–9 Ma old JdF Plate subducts toward the east-northeast beneath the North American Plate at varying rates of 30 mm/yr in the south to 45 mm/yr in the north (Kreemer et al.,

2014). Due to the curvature of the deformation front, the convergence is oblique offshore Oregon and Northern California but is close to normal offshore Washington and Vancouver Island (Figure 1).

2.1. Overriding North American Plate

The overriding North American Plate consists of several continental terranes of different origin and composition. The Wrangellia terrane in Washington and Vancouver Island and the Klamath terrane in northern California are composed of metasedimentary and oceanic crustal rocks with later silicic intrusions in a continental environment (Jones et al., 1977). Between these terranes lies the Siletz terrane, which was accreted during the Eocene and is composed of oceanic basaltic rocks interbedded with sediments (Figure 1). Based on seismic velocity and potential field data, this terrane is inferred to extend offshore between 43°N and 46°N by as much as ~40 km (Fleming & Trehu, 1999; McCrory & Wilson, 2013; Tréhu et al., 1994; Figure 1).

2.2. Propagator Wakes in the JdF Plate

The JdF Ridge has experienced eight major episodes of ridge propagation in the past 18 Ma to accommodate changes in plate motion (Karsten & Delaney, 1989; Wilson et al., 1984). A series of prominent V-shaped traces associated with the propagator wakes in the JdF Plate are identified from offset magnetic anomalies (Wilson, 2002; Figure 1a) and define the large-scale segmentation of the JdF Plate inherited from crustal formation. The inner pseudofaults, where the oceanic lithosphere in the overlap offset zone between the two ridge segments is rotated, sheared, and transferred from one plate to the other, is generally wider than the outer pseudofault on the opposite ridge flank, where the newly formed crust is juxtaposed against preexisting older crust (Hey et al., 1980; Kleinrock & Hey, 1989).

Isochrons and propagator pseudofault zones in the slab under the forearc are inferred from magnetic lineations on the conjugate Pacific Plate assuming rigid plate motion and symmetric spreading (Wilson, 2002). Within the age range of the isochrons in the slab, the spreading rate of the JdF Ridge was stable and the uncertainties resulting from asymmetric spreading are believed to be small (Wilson, 1988). In this model, no correction for slab dip has been applied (Wilson, 2002). Therefore, in regions showing large variations in slab dip, such as beneath southern Vancouver Island and Washington, the locations of the propagator pseudofault zones have larger uncertainties (Figure 1).

2.3. Presence and Distribution of Subduction Bend Faulting

Faulting deformation within the JdF Plate, attributed to complex intraplate stresses and subduction bending, has been observed to extend up to ~200 km seaward of the Cascadia deformation front from MCS data acquired prior to 2012 (Nedimović et al., 2009, and references within). These data imaged fault offsets in the sediments within the plate interior and provided evidence of increasing fault offset toward the deformation front. From MCS data acquired during the 2012 JdF Ridge-to-Trench experiment, most of the subduction bend faulting deformation is constrained to occur within ~40 km seaward of the deformation front (Han et al., 2016). Along the OR transect, which crosses the deformation front offshore central Oregon at 44.6°N, bright fault plane reflections (with dips of 40°–60°) are imaged that transect the oceanic crust and extend 6–7 km into the uppermost mantle and that are connected to large-offset faults in the sediment section. In contrast, near the deformation front offshore Washington at ~47.4°N, fault plane reflections (with dips of 60°–65°) that are confined to the upper-middle crust and connect to smaller offset faults in the sediments are imaged (Han et al., 2016). In addition, on the WA transect near the deformation front, ridgeward dipping (20°–40°) reflections are imaged in the lower crust, interpreted to be shear zones formed near the ridge axis during a period of anomalous crustal formation (Han et al., 2016). Seismic velocity models derived from OBS data along the OR transect show progressive decrease in lower crustal seismic velocities toward the deformation front associated with bending-related faulting (Horning et al., 2016). Velocity models along the trench-parallel MARGIN transect reveal a reduction in lower crustal Vp from north to south across 45.8°N, consistent with more extensive deformation and associated hydration of the incoming JdF Plate offshore central Oregon than Washington (Canales et al., 2017).

2.4. Oblique-Trending SSFs Along Cascadia Margin

Along the Oregon-Washington margin, a group of nine WNW trending left-lateral SSFs have been identified on the continental slope using side-scan sonar, bathymetry, and low-fold seismic reflection data (Appelgate

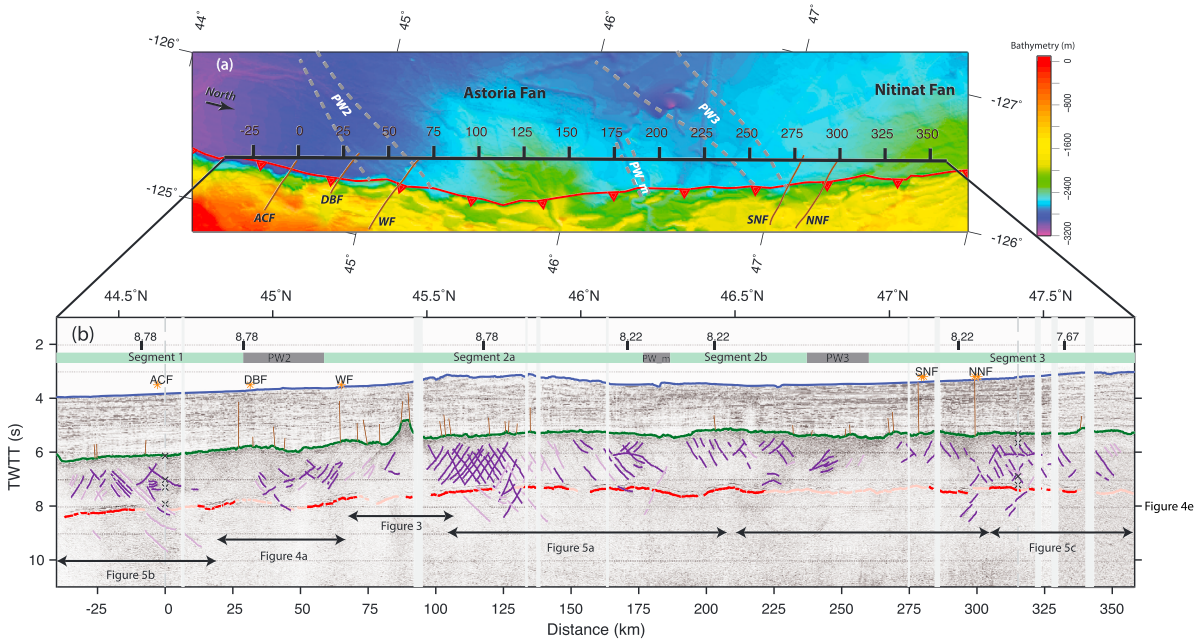

Figure 2. (a) Bathymetry from the Global Multi-Resolution Topography (GMRT) synthesis (Ryan et al., 2009) in the vicinity of the MARGIN transect. The thick black line with ticks shows the MARGIN transect with the along-track distance (km) indicated. Locations of the five major strike-slip faults (Goldfinger et al., 1997) and propagator wakes (Wilson, 2002) are marked. (b) Prestack time migrated multichannel seismic image of the MARGIN transect with interpretative line drawing superimposed. Blue and green lines are seafloor and oceanic basement respectively. Dark and light red lines indicate strong and weak Moho reflections. Interpreted Moho is shifted by 200 ms from the picked horizon to show the amplitude variation of Moho reflections along the line. Brown lines in the sediment section mark the identified faults. Dark and light purple lines show strong and weak reflections in the crust and uppermost mantle respectively. Black vertical bars with numbers at top of panel show the location of magnetic isochrons from Wilson (2002) with the plate age in Ma annotated. Horizontal gray bands show the extent of propagator wakes, while horizontal light green bands show the extent of crustal segments separated by propagator wakes. Orange stars show the location of oblique strike-slip faults previously identified from seafloor mapping (Goldfinger et al., 1997): ACF = Alvin Canyon Fault; DBF = Daisy Bank Fault; WF = Wecoma Fault; SNF = South Nitinat Fault; NNF = North Nitinat Fault. Vertical gray dashed lines at distance 0 km and 315 km indicate crossings with the OR and WA transects. Black crosses on these lines show the TWTT of crustal events identified on the OR and WA transects at crossings. Vertical light gray bars mask the data gaps associated with marine mammal mitigation. Vertical exaggeration is ~20 at seafloor. TWTT = two-way travel time.

et al., 1992; Goldfinger et al., 1992, 1997; Goldfinger, Kulm, Yeats, Appelgate, et al., 1996; Goldfinger, Kulm, Yeats, Hummon, et al., 1996). Five of these faults (from south to north: Alvin Canyon, Daisy Bank, Wecoma, South Nitinat, and North Nitinat Faults) cross the deformation front and extend to the abyssal plain with strikes of 282°–292°. These faults are estimated to be quite young, 300 to 650 ka, with total slip of 2.2 to 5.5 km. Fault traces at the seafloor are clear on the abyssal plain, barely visible on the lower slope, and become clear again on the upper slope and outermost shelf (Goldfinger et al., 1997). From the presence of basement pop-ups and sediment folds across the faults in the abyssal plain, Goldfinger et al. (1997) infer that the three Oregon faults (the Alvin Canyon, Daisy Bank, and Wecoma Faults) are slightly transpressional. The formation mechanisms of these faults and the role they play in forearc deformation are not well understood. With the geometry of the five offshore SSFs straddling the deformation front, hypotheses that faults originate in the upper plate then propagate to the lower plate or vice versa have both been proposed (e.g., Goldfinger, Kulm, Yeats, Appelgate, et al., 1996; Goldfinger et al., 1997). The left-lateral movement along these SSFs is suggested to facilitate clockwise rotation of the upper plate blocks bounded by these faults and shortening of the forearc, which may accommodate a significant amount of oblique plate convergence (Goldfinger et al., 1992, 1997; Goldfinger, Kulm, Yeats, Hummon, et al., 1996). Yet SSFs that develop in response to oblique subduction are found at other margins (e.g., Sumatra and Nankai; McCaffrey, 1991; Tsutsumi & Okada, 1996) but are commonly oriented margin-parallel rather than at a high angle to the margin as the SSFs observed at Cascadia. On land in western Oregon and Washington, numerous NW to NNW trending SSFs are observed that have been proposed to accommodate some of the clockwise rotation of the Oregon forearc documented in this region (Brocher et al., 2017). However, as these faults accommodate right-lateral motion and strike ~30°–40° more to the north compared with the offshore SSFs, it is unclear whether or how they are related to the offshore SSFs.

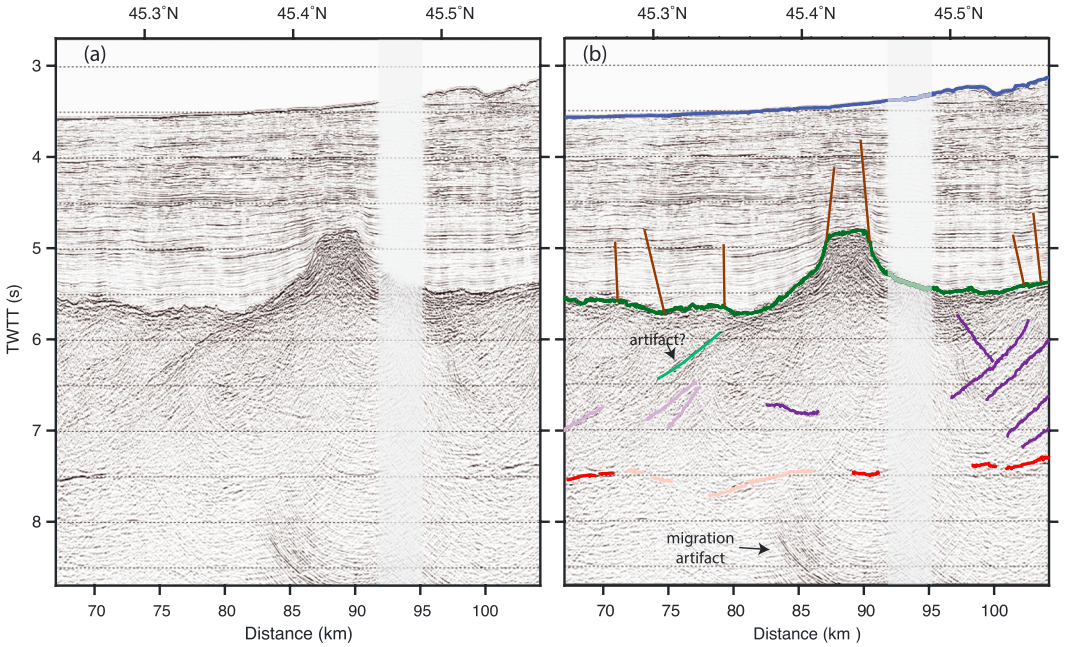

Figure 3. Seamount 1.2 km high and 15.3-km wide imaged along MARGIN transect. (a) Uninterpreted and (b) interpreted prestack time migration images. The color code of the interpreted lines is the same as Figure 2. Vertical exaggeration is ~9.3 at seafloor. Based on the analysis described in the supporting information, one dipping event near the base of the seamount might be an out-of-plane artifact. TWTT = two-way travel time.

3. Data and Methods

The trench-parallel MARGIN transect of Ridge-to-Trench experiment spans ~400 km along the margin from 44.3°N, 125.3°W to 47.8°N, 126.4°W. Most of this transect is located ~10–20 km seaward of the deformation front, except south of 44.6°N where the profile reaches within 5 km of the deformation front (Figures 1, 2a, and S1 in the supporting information).

The MCS data were acquired aboard the R/V *Langseth* using a 6,600 cubic inch (108 L) airgun array towed at a nominal depth of 9 m and fired every 37.5 m. The data were recorded with an 8-km solid streamer with 636 active hydrophone groups towed at a nominal depth of 9 m. The positions of sources and receivers were derived from Global Positioning System sensors located on the ship, on the airgun arrays and the streamer tail-buoy, and using 26 compass-enhanced DigiCourse birds deployed along the streamer. Shot data were recorded with a sampling rate of 2 ms for 12.28-s-long records. Several data gaps with widths of 0.7–3.4 km are present on this line due to airgun shut downs/power downs during marine mammal sightings (Figures 2b and S2).

Processing of the MCS data follows a similar sequence as for the OR and WA Transects, which is described in detail in Han et al. (2016) and is summarized here. To account for streamer feathering, a pseudo 3-D geometry is defined and the data are sorted into common midpoint bin gathers that are 6.25 m wide in the profile direction. Band-pass filtering (3-7-220-250 Hz) is applied to remove cable noise, followed by trace editing, spherical divergence correction, resampling to 4 ms, and despiking using the LIFT method (Choo et al., 2004). Predictive deconvolution is used to collapse the airgun source bubble pulse reverberations. Along much of our line, the seafloor and sediment layer multiples arrive earlier than the Moho reflection and obscure part of the lower crust, Moho, and uppermost mantle section. We applied Radon filtering, which effectively removes these multiples and reveals the deeper structure. Kirchhoff prestack time migration (PSTM) is applied using velocity models for the sediment section derived from semblance analysis at 200 common midpoint intervals and the crustal/mantle velocities derived from OBS data of the coincident line (Canales et al., 2017). The final PSTM velocity model is used for depth conversion. Time varying gain is applied for display purposes.

From our reflection images (Figures 2–5), seafloor, top of oceanic crust, and Moho are identified and digitized to derive sediment thickness and crustal thickness (Figure 6). With an averaged *P* wave velocity uncertainty of

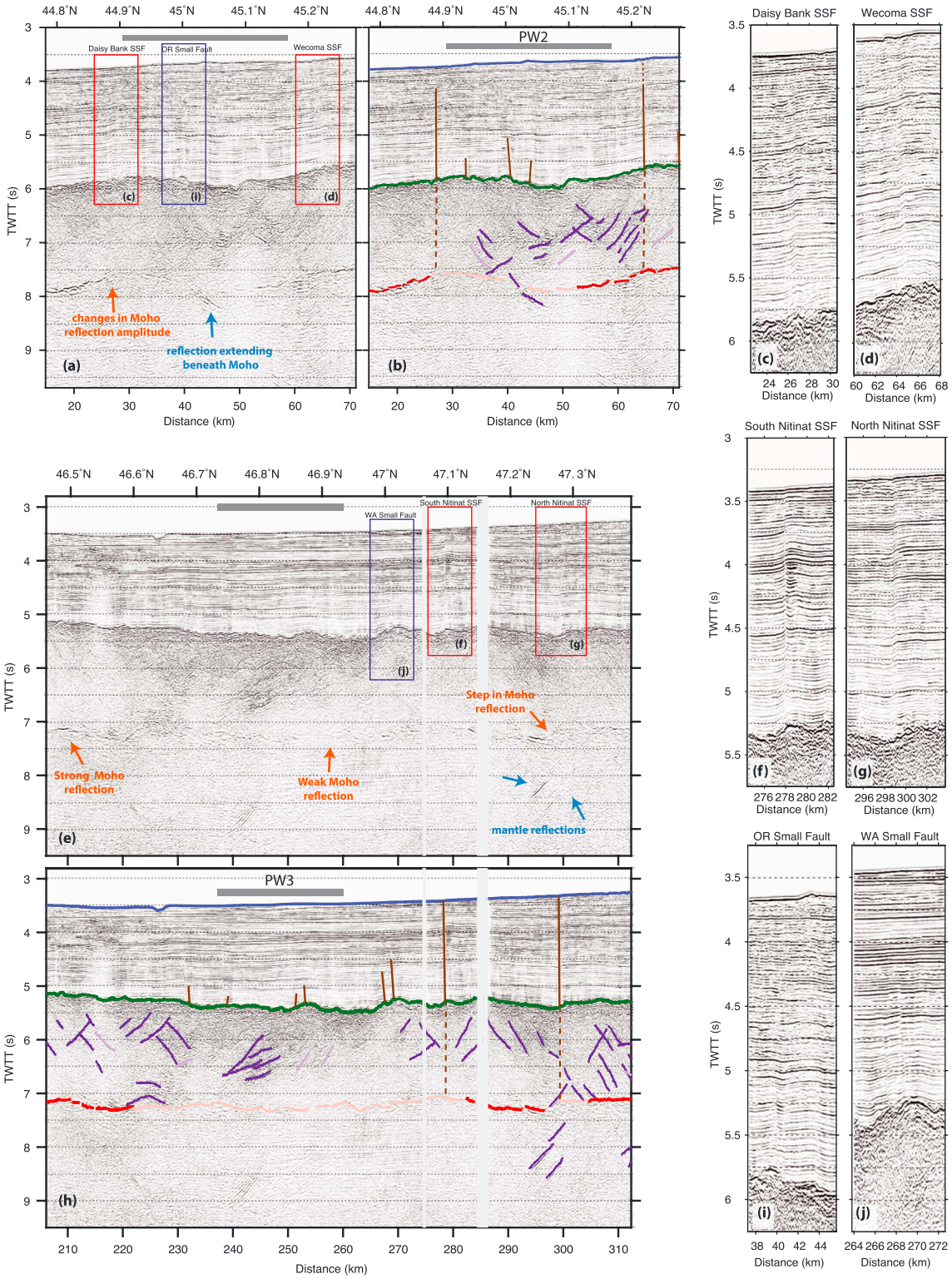

Figure 4. Structure of propagator wakes and strike-slip faults. (a) Uninterpreted and (b) interpreted prestack time migration images of the Juan de Fuca Plate near propagator wake PW2. Horizontal gray bands show the extent of propagator wakes. Changes in Moho reflection and dipping reflections are indicated. Inset: two major strike-slip faults (Daisy Bank and Wecoma Faults) and two small steeply dipping faults in this region are shown in (c), (d), and (i). (e) Uninterpreted and (h) interpreted prestack time migration image of the Juan de Fuca Plate near propagator wake PW3. Inset: two major strike-slip faults (South Nitinat and North Nitinat Faults) and two small steeply dipping fault in this region are shown in (f), (g), and (j). The color code of the interpreted lines is the same as Figure 2. Vertical exaggeration is ~13 at seafloor. TWTT = two-way travel time; SSF = strike-slip fault.

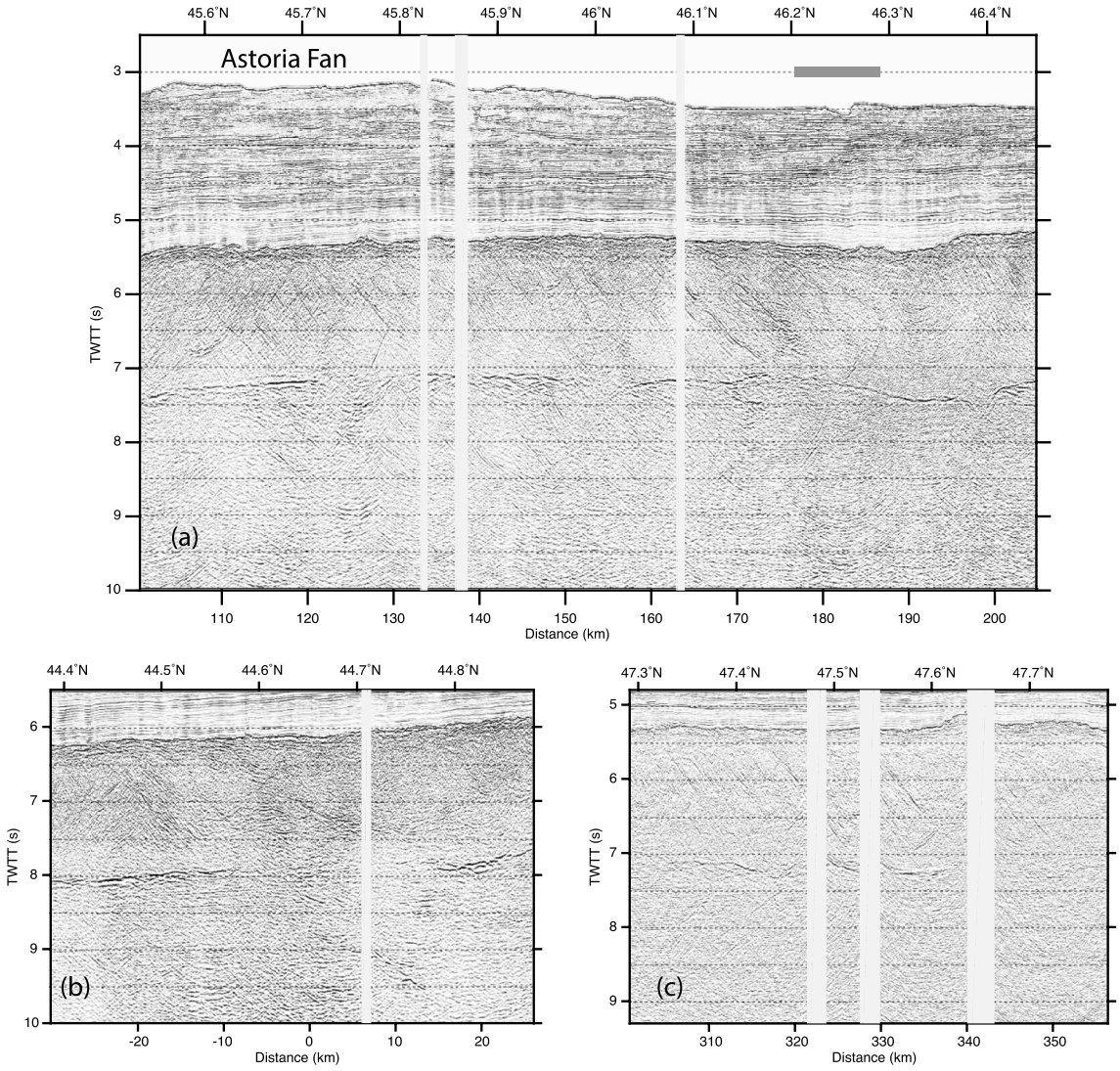

Figure 5. Variations in crustal reflectivity. (a) Uninterpreted and (d) interpreted prestack time migration (PSTM) images of crustal Segment 2 where intracrustal reflectivity changes from antithetic reflections in the south to northward dipping reflections in the north. Also note the variation of sediment reflection characteristics from the center of Astoria fan to further north. (b) Uninterpreted and (e) interpreted PSTM images of crustal Segment 1 where northward and southward dipping reflections are observed. (c) Uninterpreted and (f) interpreted PSTM images of crustal Segment 3 where crustal reflections are dominantly northward dipping. The color code of the interpreted lines is the same as Figure 2. Vertical exaggeration is ~11.5 at seafloor. TWTT = two-way travel time.

~±5% for the sediments and ±0.15 km/s for the crust (Canales et al., 2017), uncertainties in sediment and crustal thickness estimates are ±70 to 150 and ± 120 to 200 m, respectively. In addition to the major horizons, our reflection images reveal fault offsets in the sediment section as well as abundant reflections in the crust, some extending into the uppermost mantle. Faults in the sediment section are identified from steps, breaks, and deflection of sedimentary layers. The data resolution permits identification of fault offsets of ~3–5 m in the shallow sediments (dominant frequency 40–60 Hz) and 7–13 m near the top of oceanic crust (dominant frequency 35–55 Hz).

Through PSTM, seismic energy from genuine crustal/mantle reflections is well focused using crustal/mantle velocities, whereas out-of-plane arrivals from seafloor or basement, which propagate through regions of lower root-mean-square velocity, cannot be well focused. Therefore, any intracrustal and intramantle events present after PSTM processing can be interpreted as true reflections within the crust and uppermost mantle. To further validate the nature of the intracrustal/mantle reflectivity, we applied an independent processing

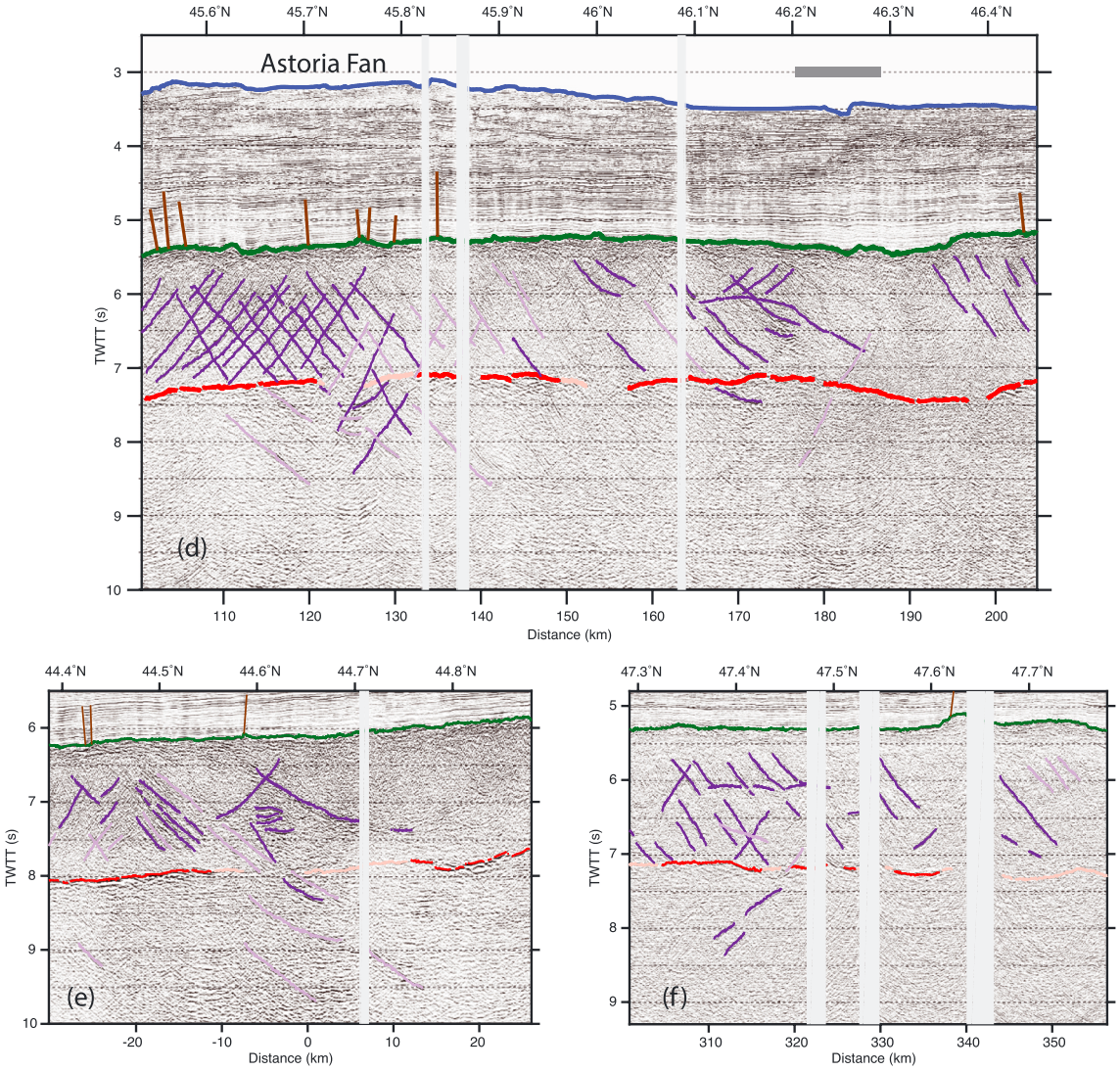

Figure 5. (continued)

flow involving dip-moveout with water or basement root-mean-square velocity, F-K filtering, and poststack time migration. This analysis approach has been used to eliminate contamination from out-of-plane seafloor or basement reflections in previous studies of oceanic crust (Calvert, 1995; Canales et al., 2005; Kent et al., 1996; Ranero et al., 1997; Reston et al., 1999; supporting information Figure S3). Most of the events present on images obtained through this approach are consistent with those in our PSTM images, confirming that these events are genuine intracrustal/mantle reflections. In our interpretation of these reflections, only events with length greater than 1 km are digitized. Adjacent events are picked as separate events if separated in time by more than 80 ms (corresponding to twice the period of the dominant frequency of 25 Hz). The apparent dips of faults in the sediment and of the crustal and mantle reflections are measured from the depth-converted images.

4. Results: Sediment, Crustal, and Uppermost Mantle Structure

In this section results from the PSTM images and depth-converted interpretations (Figures 2–6) from our MARGIN transect are described. Distances along the transect are measured from an origin defined as the intersection with the OR transect at ~44.65°N, 125.45°W. Our line crosses two major propagator wakes (PW2 and PW3) with along-track widths of 30 and 23 km, and age offsets of 0.6 and 0.9 Ma, respectively. An additional pseudofault from a smaller, short-lived propagating offset (along-track width: 10 km and age

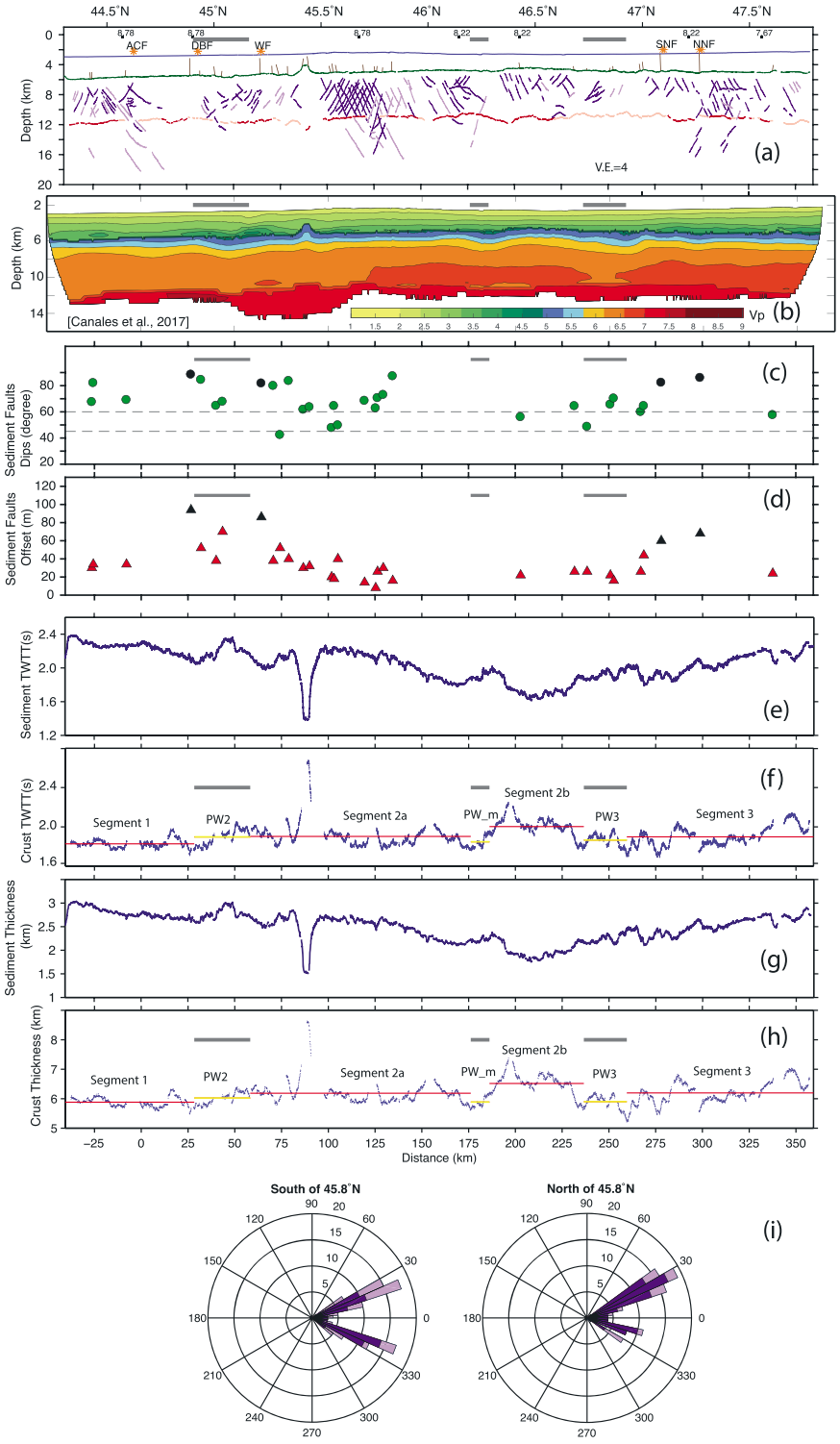

Figure 6. Along-strike structural variations of the JdF Plate along the MARGIN transect. (a) Interpretative line drawing from the depth-converted section. The color code is the same as Figure 2. (b) Seismic velocity determined from wide-angle reflection and refraction data (Canales et al., 2017). (c) Apparent dips of faults in the sediment section. Black circles indicate the dips of major strike-slip faults. (d) Vertical offset of faults in the sediment section. Black triangles indicate the offsets of the major strike-slip faults. (e) Sediment thickness in two-way travel time (TWTT) along the transect. (f) Crustal thickness in TWTT. The horizontal red and yellow lines show the average crustal TWTT within crustal segments and propagator wakes, respectively. (g) Sediment thickness from depth converted section. (h) Crustal thickness from depth converted section. The horizontal red and yellow lines show the average crustal thickness within crustal segments and propagator wakes, respectively. (i) Apparent dip distribution of intracrustal and upper mantle reflections south and north of 45.8°N (distance 135 km). ACF = Alvin Canyon Fault; DBF = Daisy Bank Fault; WF = Wecoma Fault; SNF = South Nitinat Fault; NNF = North Nitinat Fault.

offset: 0.3 Ma) in between PW2 and PW3 is also crossed (labeled as PW_m, for minor propagator wake). All three are inner pseudofaults with the young crust side located to the south. They divide the JdF Plate into four segments (numbered 1, 2a, 2b, and 3 from south to north; Figure 2).

4.1. Sediment Section

Excluding the area in the vicinity of a buried seamount (Figures 2 and 3), the thickness of the sediment section above the oceanic crust ranges from 1,610 to 2,390-ms two-way travel time (TWTT; 1.8–3.0 km thick) with thicker sediments observed where the survey line is closer to the deformation front (distance −40–0 km) and near the central region of the Astoria Fan (distance 90–165 km) and Nitinat Fan (distance 310–360 km; Figures 2, 6e, and 6g). The lower portion of the sediment section (~1,000-ms TWTT and 1.4-km thick) is generally well layered, whereas the reflection characteristics of the upper sediment section vary with proximity to the fans (Figures 2 and S2). Far from the Astoria Fan, the upper sediment section is highly reflective with irregular layering in places (Figure 4). Near the center of the Astoria Fan the reflection amplitude of the sediment section varies greatly with semitransparent packages and, in places, chaotic discontinuous reflections embedded within bright subhorizontal layers (Figures 5a and 5d).

Along the MARGIN transect, 31 faults are identified in the sediments based on the criteria described in section 3 (Figure 2b). The most prominent of these faults are the four left-lateral oblique-trending SSFs crossed by our line that have been previously identified (Figure 1): Daisy Bank, Wecoma, South Nitinat, and North Nitinat Faults (Figures 4c, 4d, 4f, and 4g). The Alvin Canyon Fault also belongs to this group, but no surface fault trace has been observed beyond 7 km seaward of the deformation front (Goldfinger et al., 1997), and no offsets are imaged in the sediment section at the westward projection of this fault to our line. The four SSFs are steeply dipping (82°–88°, Figures 4 and 6c) are associated with the largest vertical offsets measured for all the intrasedimentary faults identified (85–95 m for Daisy Bank and Wecoma Faults and 60–70 m for South and North Nitinat Faults) and can be traced to/near the seafloor (Figures 4 and 6d). Of them, North Nitinat, South Nitinat, and Wecoma Faults are associated with small seafloor steps of 8–12 m. Along the fault planes, breaks of sediment layers are not always observed; rather, the sediment layers usually curve upward or downward near the fault zone (Figures 4c, 4d, 4f, and 4g). Compared with these major SSFs, the other faults identified in the sediment section are much smaller in offset and disrupt less of the sediment section. These faults display vertical offsets that are generally less than 40 m, with no offsets resolved in the sediment section shallower than 1,000-ms TWTT (~1.4 km) above the basement, and most are associated with basement offsets (Figures 4i, 4j, and 6d). Almost all of these faults have apparent dips larger than 45°, and about 75% of them have steep apparent dips larger than 60° (Figure 6c).

4.2. Oceanic Crust and Uppermost Mantle

The top of the oceanic crust is a strongly reflective interface along the full extent of the profile (Figures 2–5). A seamount, 1.2 km high above the regional basement depth, is imaged centered at distance 88 km (125.69°W, 45.43°N). This seamount is 15.3-km wide at its base and has a 2.7-km-wide flat top bounded by faults in the sediments that extend to 0.32 km beneath the seafloor (Figure 3). This seamount may belong to the group of seamounts that have been inferred from sea surface magnetic and gravity data beneath Cascadia forearc between 44°N and 45°N (Tréhu et al., 2012). Wide basement depressions (~30–50-km wide) with maximum relief of 540, 480, and 390 m relative to surrounding basement are observed at the locations of the three propagator wakes (Figures 2, 4, and 7). At short wavelengths (~10 km), the basement is comparatively smooth with variations in relief of ~50 m.

Moho reflections of variable amplitude can be traced along most of our transect (Figures 2 and S2). A weak Moho is imaged beneath PW2, PW3, and the seamount. Local regions of reduced Moho reflection amplitude are also found in several regions where dipping reflections extending to the mantle are observed (e.g., −5 to ~5 km, near 125 km, Figure 2). It is noteworthy that changes in Moho reflections are observed across most of the major SSFs: Moho reflection is disrupted with a travel time step of 180 ms (~0.6 km) across the North Nitinat Fault and changes abruptly from strongly reflective to weakly reflective across the Daisy Bank Fault and near the South Nitinat Fault (Figure 4).

Crustal thickness is on average 1,900 ± 110-ms TWTT (6,150 ± 380 m) with small variations (~10%) between crustal segments and within propagator wakes (Table 1 and Figures 6f and 6h). Segment 1 has the thinnest crust (1,830 ± 40-ms TWTT, 5,880 ± 160 m), while Segment 2b has the thickest crust

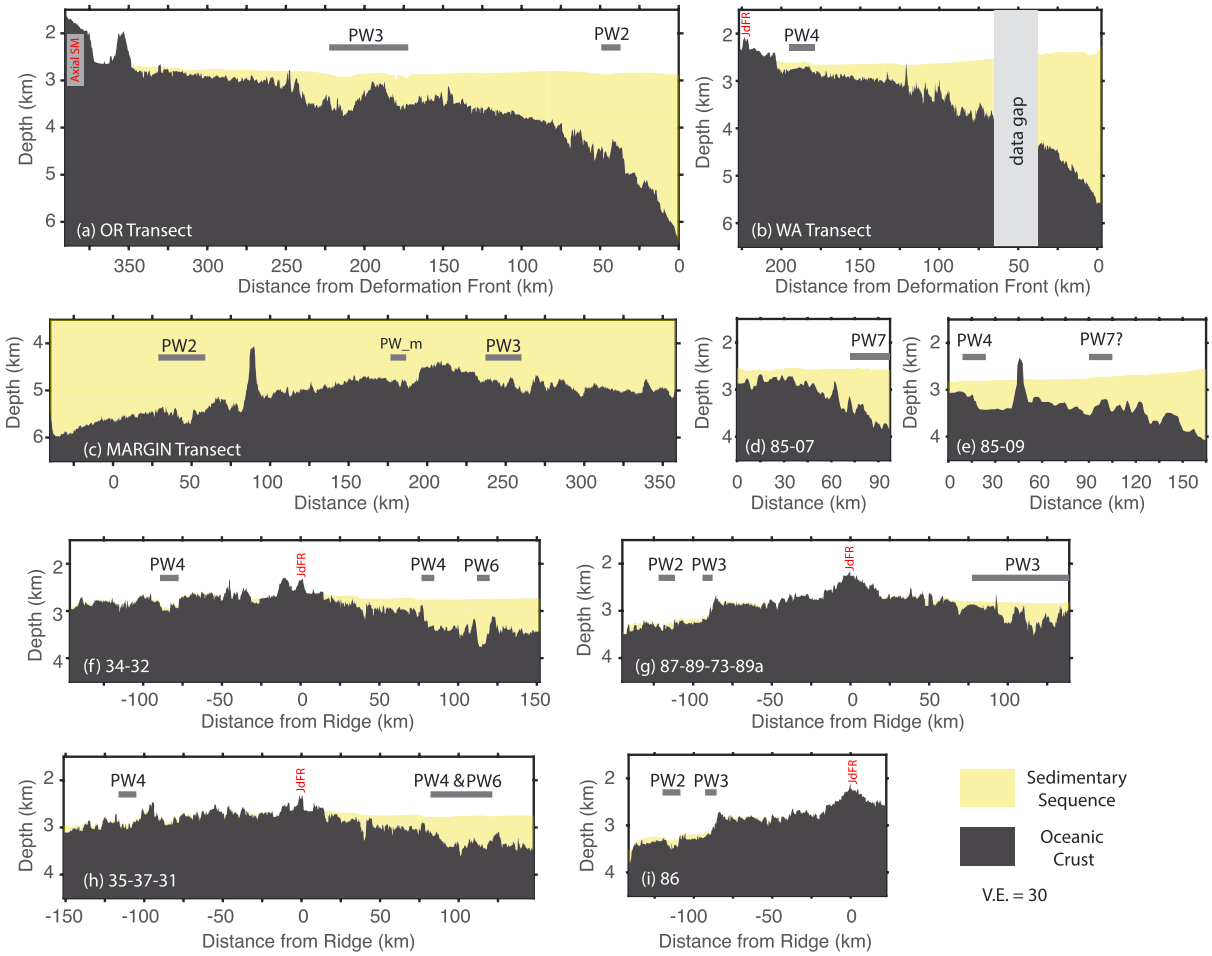

Figure 7. Compilation of basement topography near propagator wakes. Depth converted seismic profiles shown are the OR, WA, and MARGIN transects (a–c) from the JdF Ridge-to-Trench experiment (Han et al., 2016, this study), lines 85-07 and 85-09 (d and e) from a 1985 Canadian survey (Calvert et al., 1990; Hasselgren & Clowes, 1995), and lines 34-32, 87-89-73-89a, 35-37-31, 86 (f–i) from survey EW0207 (Carbotte et al., 2008). Locations of these profiles are shown in Figure 1a. Sections are shown with vertical exaggeration of 30 in order to highlight the basement relief. SM = Seamount.

(2,000 ± 90-ms TWTT, 6,510 ± 340 m). While the crust within PW_m and PW3 is thinner than adjoining crustal segments by 300–600 m, the average crustal thickness within PW2 is intermediate between that of the adjoining segments (Table 1).

Along our profile, numerous dipping events of variable apparent dips and amplitude are imaged in the crust and a few of them in the uppermost mantle (Figures 2–6). In general, crust south of 45.8°N (distance 135 km) is more reflective with southward and northward dipping reflections extending to the lower crust. In comparison, the crust to the north is less reflective with dominantly northward dipping events confined largely to the upper-middle crust (Figures 2 and 5). In Segment 1, antithetic dipping reflections are observed from distance −40 to −12 km above a strongly reflective Moho (Figures 2, 5b, 5e, and 6a). A strong shallowly dipping (~10°) reflection and several short subhorizontal reflections are imaged near the crossing point with the OR transect (from distance −10 to 10 km). A group of northward dipping reflections that transect the Moho and extend to 6–7 km beneath the weakly reflective Moho are also observed (Figures 5b and 5e). Within PW2, clusters of synthetic northward and southward dipping reflections that bound the wake are imaged (Figures 4a and 4b). In Segment 2, from distance 100–135 km, the crust displays strongly reflective antithetic events spaced 1–4 km apart with dominant apparent dips of 25°–30°. Beneath these crisscross reflections, some faint mantle reflections are observed with similar apparent dips extending to ~5–6 km beneath the Moho (Figures 5a, 5d, and 6a). North of distance 135 km within Segment 2, crustal reflections are dominantly northward dipping. Most crustal reflections are confined to within the upper 1,300–1,400 ms (~3.5–4 km) of the crust and very

Table 1
Average Crustal Thickness of JdF Plate Segments and Propagator Wakes Derived From R2T MCS Data

	Segment 1			Segment 2			Segment 3		
Seismic lines	TWTT (ms)	Depth (m)	Sampling line length (km)	TWTT (ms)	Depth (m)	Sampling line length (km)	TWTT (ms)	Depth (m)	Sampling line length (km)
MARGIN	1,830 ± 40	5,880 ± 160	69.0	1,900 ± 120 (2a) 2,000 ± 90 (2b)	6,180 ± 400 (2a) 6,510 ± 340 (2b)	117.9 (2a) 50.5 (2b)	1,900 ± 100	6,200 ± 370	97.5
OR	1,780 ± 80	5,740 ± 170	37.0	1,930 ± 100	6,170 ± 230	122.9	—	—	—
WA	—	—	—	—	—	—	2,000 ± 90	6,440 ± 270	179.0
Average weighted by line lengths	1,810	5,830		1,930	6,230		1,960	6,360	

Note. MCS = multichannel seismic; TWTT = two-way travel time.

few mantle reflections are identified (Figures 2, 5a, 5d, and 6a). Within PW3, southward dipping reflectors are imaged in the middle crust. It is noteworthy that most of the southward dipping reflections in the crust north of 135 km are located within propagator wake crust (Figures 2, 4e, 4h, and 6a). In Segment 3, northward dipping upper crustal reflections (dominant apparent dips ~20–30°) are imaged along with a few weak subhorizontal events at ~750–800 ms (~2.1–2.3 km) beneath basement and a group of northward dipping lower crustal reflections (Figures 2, 5c, 5f, and 6a). A few bright shallowly dipping (apparent dips 18–23°) reflections are imaged within 1,200 ms (4–5 km) of the uppermost mantle, beneath the Moho step associated with northern Nitinat fault (Figures 4e, 4h, and 6a).

5. Interpretation of Crustal and Mantle Reflections

To evaluate the origin of the intracrustal and intramantle reflections observed on our MARGIN line, we compare the apparent dips of these events with the range expected if they arise from the normal faults in the oceanic crust/mantle or from the lower crustal ridgeward dipping reflectors (LCR) imaged on the OR and WA transects and previously described in Han et al. (2016; Figure S4).

For a 3-D dipping plane sampled by a 2-D line, its apparent dip on the 2-D line is a function of the true dip of the plane and the difference between the orientation of the 2-D line and the strike of the dipping plane (equation (1)).

$$\tan\gamma = \tan\alpha \cdot \sin\theta, \tag{1}$$

in which γ is the apparent dip, α is the true dip, and θ is the difference between the strike of the 2-D line and the strike of the dipping plane.

From seismic reflection and bathymetry data in several subduction zones around the Pacific and Indian Oceans, Masson (1991) observes that preexisting abyssal hill normal faults are reactivated under subduction bending if the spreading fabric is less than 25°–30° from the strike of the trench, whereas new trench-parallel bending-related normal faults are formed if the spreading fabric is >25°–30° oblique to the trench. South of 45°N, the trench is at low angle with the spreading fabric (Figure S1), and we assume that the dominant strike of bending-related normal faults in this region follows the strike of magnetic isochrons. Further to the north, the spreading fabric is at 20°–30° to the trench (Figure S1), and we assume that both trench-parallel and spreading fabric parallel bending faults could form (Masson, 1991). Therefore, the expected strike difference between these faults and the MARGIN line is 15°–25° for most of the line with a total range of 0°–30° (Figure S1). As both the OR and WA lines are oriented nearly perpendicular to magnetic isochrons, dips of 40°–65° measured for fault reflections in the upper/middle crust on the WA line and through the crust on the OR line are assumed to represent the range of true dips for these normal faults. If the reflectivity observed on the MARGIN line arises from these normal faults, apparent dips of 12°–40° are predicted for most of the line with a predicted total range of 5°–45° (Figure S4). Our observed apparent dips of ~20°–30° fall in this range (Figure 6i).

Along the WA transect near where it crosses our MARGIN line, lower-crustal reflections with shallower dip angles of ~20°–40° are imaged beneath the upper/midcrustal normal faults (Han et al., 2016). Assuming that these reflections arise from structures (shear zones) that also strike parallel to magnetic isochrons, predicted

Table 1 *(continued)*

	PW2			PW_m			PW3		
Seismic lines	TWTT (ms)	Depth (m)	Sampling line length (km)	TWTT (ms)	Depth (m)	Sampling line length (km)	TWTT (ms)	Depth (m)	Sampling line length (km)
MARGIN	1,900 ± 80	6,020 ± 210	29.9	1,850 ± 60	5,880 ± 170	10.0	1,870 ± 60	5,900 ± 230	23.0
OR	1,890 ± 110	5,900 ± 250	12.3	—	—	—	1,910 ± 90	6,010 ± 170	50.3
WA	—	—	—	—	—	—	—	—	—
Average weighted by line lengths	1,900	5,990		1,850	5,880		1,900	5,980	

apparent dips are ~5°–25°, which are at the low end of the observed range of reflector dips (20°–30°). From these comparisons, and the observation that dipping events on the MARGIN line north of distance 135 km are mostly confined to the middle crust, our favored interpretation is that most of the events imaged on the northern half of the MARGIN line coincide with the upper/midcrustal normal faults, and the LCRs are not well imaged. If the few lower crustal dipping reflections imaged near distance 310 km are from the LCRs, the small deviation from predicted apparent dips may reflect that the strike of the LCR events are not parallel to spreading fabrics. As observed in the Cocos Plate in the eastern Pacific, only 40% of the lower crustal reflections are subparallel (±30°) to the paleoridge axis (Scott & Henstock, 2016).

In summary, from the apparent dips of the crustal/mantle reflections on the MARGIN line along with observations from the two crossing lines we conclude that most of the dipping reflections imaged are consistent with normal faulting within the oceanic crust.

6. Discussion

6.1. Segmentation of the JdF Plate Defined by Propagator Wakes and Its Effect on Plate Interface Slip Behavior

6.1.1. Structure of Propagator Wakes and Crustal Segments From MARGIN Transect

Our PSTM images from the MARGIN transect indicate anomalous crustal structures associated with the propagator wakes. The long-wavelength larger-amplitude basement reliefs of 390–540 m within and in the vicinity of the three propagator wakes constitute significant topographic anomalies on an otherwise low-relief basement (Figure 7). Weak Moho reflections are imaged beneath PW2 and PW3 (Figures 2b, 4a, 4b, 4e, 4h, and S2). At PW3 Canales et al. (2017) report subdued *Pg-PmP-Pn* triplications (indicative of gradual transition from crustal to mantle velocities) and Vp of 7.7 km/s for the uppermost mantle (~0.2 km/s slower than the mantle Vp expected after correcting for mantle anisotropy; Figure 6b), coincident with our observation of weak Moho reflections (Figures 4e and 4h). Propagator PW2, which displays strong Moho reflections at wake boundaries and weak Moho reflections in the middle region of the wake (Figures 4a and 4b), is anomalous in the sense that it is associated with a variable mantle velocity (7.7–8.1 km/s) and an anomalous azimuthal anisotropic signature that cannot be explained by simple fast-axis alignment of olivine crystals along the paleospreading direction (Canales et al., 2017; Figure 6b). Along the OR transect, which crosses PW2 and PW3 further west in the plate interior (Han et al., 2016), similar weak Moho reflections are observed that coincide with reduced upper mantle velocity (as low as 7–7.2 km/s), weak wide-angle *PmP* reflections, and subdued *Pg-PmP-Pn* triplications (Horning et al., 2016). Interestingly, crustal reflectivity characteristics of the propagator wakes are markedly different on the OR transect compared with the MARGIN transect: while the crust of PW2 and PW3 is mostly seismically transparent on the OR transect, dipping reflections are imaged within the crust at both propagator wakes along the MARGIN transect.

Our data indicate small differences in crustal thickness between the different crustal segments separated by the propagator wakes. In Table 1, we compile average crustal travel times for Segments 1, 2, and 3 along all three transects from the ridge-to-trench survey and corresponding thicknesses obtained using coincident Vp models derived from OBS tomography (Canales et al., 2017; Horning et al., 2016). The average crustal travel time and thickness ranges from 1,780 ± 80 ms (5,740 ± 170 m) to 2,000 ± 90 ms (6,510 ± 340 m), with the thinnest crust measured at the southernmost Segment 1 and thickest at subsegment 2b. Averaging of

measurements obtained along all three transects provides an average crustal thickness for Segment 1 (5,830 m) that is 7–9% less than that for Segment 2 (6,230 m) and Segment 3 (6,360 m), indicating a regional pattern of lower mantle magma supply to the southern segments during crustal formation.

6.1.2. Comparison of Seismic Observations of Propagator Wakes on the JdF Plate

The structural characteristics of propagator wakes obtained from the Ridge-to-Trench experiment (Canales et al., 2017; Han et al., 2016; Horning et al., 2016; this study) and from previous seismic reflection (1985 and 2002) and refraction (1985) surveys conducted on the JdF Plate (Calvert et al., 1990; Carbotte et al., 2008; Hasselgren et al., 1992; Hasselgren & Clowes, 1995; McClymont & Clowes, 2005; Nedimović et al., 2005) are compared in Table 2 and Figure 7. This compilation reveals several common features: (1) Propagator wakes typically coincide with anomalies in basement topography, including local lows, highs, and abrupt topographic steps. The amplitude of these topographic anomalies ranges from 250 to 740 m (encompassing the range observed in our study), which is higher than the typical basement relief away from propagators (~70 m for crust age of 1–3.2 and 6–8.78 Myr, ~200 m for crust age of 3.2–6 Myr; Boulahanis et al., 2015). (2) Most propagator wakes are associated with absent or weak Moho reflections. (3) Reduced Vp in the lower crust and/or uppermost mantle is observed on all three propagator wakes that have been sampled by seismic refraction data. (4) Sub-Moho reflectivity is observed beneath/near outer pseudofaults but is absent beneath/near inner pseudofaults. (5) Propagator wake crust is typically transparent on seismic lines that are oriented perpendicular to seafloor magnetic isochrons, whereas intracrustal reflections are detected in these zones on lines that run at low angles to the seafloor spreading fabric.

These properties are likely all inherited from the ridge propagation process. Outer pseudofaults are generally associated with basement steps where shallower depths are found on the young crust side, as expected at these offsets where crust of different ages is juxtaposed. Inner pseudofaults are typically associated with basement lows, sometimes bounding intervening highs, consistent with the expected shearing and rotation of crustal blocks between the propagating and retreating ridge tips (Figure 7). The orientation-dependent imageability of crustal reflectivity within the propagator wakes may reflect the difference in the orientation of crustal fabric within the wakes from that of the adjoining crustal segments (Kleinrock & Hey, 1989). A seismic line that strikes perpendicular to spreading isochrons will be at low angles to rotated crustal fabric within the propagator wakes, making it difficult to image the fault planes within the propagator wakes, and vice versa.

Most of the propagator wakes from the JdF Plate are associated with absent or weak Moho reflections (Table 2) and anomalous *Pg-PmP-Pn* triplications where wide-angle data are available (Canales et al., 2017; Horning et al., 2016), suggesting a reduced impedance contrast between the lower crust and the uppermost mantle, and/or that the crust/mantle transition zone is too thick and gradual with respect to the dominant wavelength of the imaging seismic wave at these depths for a reflection to be generated. Seismic refraction data are available from three pseudofault zones (PW2, PW3, and PW7, Figure 1) and Vp as low as 7–7.2 km/s in the uppermost mantle has been reported (Horning et al., 2016; McClymont & Clowes, 2005). Two mechanisms can reduce Vp at uppermost mantle depths: fracturing with fluid penetration, which increases the potential for mantle serpentinization (McClymont & Clowes, 2005), and crustal underplating caused by propagation-related magmatism (Calvert et al., 1990). From forward modeling of gravity data across PW7, McClymont and Clowes (2005) conclude that the observed gravity anomalies are better explained by presence of serpentinized mantle rather than thickened gabbroic lower crust. Across PW3, Canales et al. (2017) explain the Vp reduction as mostly due to fluid-filled cracks, with mantle serpentinization playing a secondary role due to the high temperatures predicted given the young age of the plate. We thus favor the interpretation that the lower crust and uppermost mantle at propagator wakes are regions of variably reduced Vp arising from fracturing and locally spatially variable hydration of the mantle.

Sub-Moho reflectivity that is subhorizontal or shallowly dipping has been observed near the outer pseudofaults of PW4 and PW7 on the JdF Plate and the outer pseudofault of PW3 on the Pacific Plate and is interpreted to result from freezing of propagation-related magma bodies at the base of the crust (Calvert et al., 1990; Nedimović et al., 2005). No such reflectivity is identified near the corresponding inner pseudofaults (Calvert et al., 1990; Nedimović et al., 2005) or near the inner pseudofaults of PW2 and PW3 on the JdF Plate sampled by the JdF Ridge-to-Trench transects (Han et al., 2016). These differences may reflect the different deformational regimes associated with inner and outer pseudofault zones. Unlike crust within the inner wakes, which is rotated and sheared, crust within outer propagator wakes experiences little

Journal of Geophysical Research: Solid Earth

10.1002/2017JB015059

Table 2
Characteristics of Propagator Wakes on the JdF Plate and Their Counterparts on the Pacific Plate

PW #	Plate	PW type	Seismic transect	Data acquisition year	Seismic line orientation wrt nearby isochrones	Sample location	Basement topography	Moho reflection	Intracrustal reflectivity	Sub-Moho reflectivity	Vp
2	JdF	Inner	OR-transect	2012	90°	44.8°N, 125.9°W	Topographic high of ~360 m over an ~8-km wide block (1)	Weak (1)	Absent except sparse weak fault plane reflections in the upper crust (1)	Absent (1)	Moderately reduced Vp (~0.1 km/s) in the lower crust; significantly reduced Vp (~1 km/s) in the uppermost mantle (Vp: 7–7.2 km/s) (2)
			MARGIN-transect	2012	0°–18°	45.0°N, 125.6°W	Topographic low with maximum relief of 540 m (3)	Weak (3)	South and northward dipping reflections are present in the middle and lower crust (3)	Absent (3)	PW coincides with local Vp minimum in the lower crust. Mantle Vp reduces from 8.1 km/s to 7.7 km/s from young crust side to old crust side within PW, and further reduced to 7.5 km/s north of the PW (4)
	PA	Outer	87-89-73-89a	2002	80°–90°	45.2°N, 131.6°W	Topography low with maximum relief of 220 m (5)	Absent (6)	Absent (5)	Absent (6)	—
			86	2002	80°–90°	45.1°N, 131.6°W	Topography low with maximum relief of 300 m (5)	Absent (6)	—	Absent (6)	
3	JdF	Inner	OR-transect	2012	90°	45.3°N, 127.7°W	Topographic anomaly over 50-km wide: Topographic high bounded by troughs with total relief of 740 m (1)	Weak (1)	Absent (1)	Absent (1)	Moderately reduced Vp (~0.1 km/s) in the lower crust; significantly reduced Vp (~1 km/s) in the uppermost mantle (Vp: 7–7.2 km/s) (2)
			MARGIN-transect	2012	24°–28°	46.8°N, 126.1°W	Topographic low with maximum relief of 390 m (3)	Weak (3)	Dominantly southward dipping reflections are present in the middle crust (3)	Absent (3)	PW coincides with local Vp minimum in the lower crust. Mantle Vp within the PW is 7.7–7.8 km/s (4)
			87-89-73-89a	2002	90°	44.5°N, 128.9°W	Wide topographic low with local high blocks. Maximum relief ~650 m (5)	Absent to moderate, with localized strong reflection (6)	Absent (5)	Absent (6)	—
	PA	Outer	87-89-73-89a	2002	90°	45.1°N, 131.3°W	Basement steps down from young crust side to old crust side with maximum relief of ~510 m (5)	Absent to moderate (6)	Absent (5)	Sub-Moho reflection is imaged on the young crust side (6)	—
			86	2002	90°	45.1°N, 131.3°W	Basement steps down from young crust side to old crust side with maximum relief of ~500 m (5)	Absent (6)	—	Sub-Moho reflection is imaged on the young crust side (6)	
4	JdF	Outer	17-3-1 (WA transect)	2002	90°	47.8°N, 128.6°W	Basement steps down from young crust side to old crust side with maximum relief of ~250 m (5)	Weak to moderate (6)	Absent (6)	Sub-horizontal reflection is imaged beneath Moho on the young crust side, with lateral extent of ~4–5 km and combined thickness ~ 2 km (6)	—

Journal of Geophysical Research: Solid Earth

10.1002/2017JB015059

Table 2 *(continued)*

PW #	Plate	PW type	Seismic transect	Data acquisition year	Seismic line orientation wrt nearby isochrones	Sample location	Basement topography	Moho reflection	Intracrustal reflectivity	Sub-Moho reflectivity	Vp
			34–32	2002	90°	46.5°N, 128.2°W	Basement steps down from young crust side to old crust side with maximum relief of ~450 m (5)	Moderate to strong (6)	Absent (5)	Sub-Moho reflection is imaged on the young crust side (6)	—
			35-37-31	2002	90°	46.3°N, 128.2°W	Basement steps down from young crust side to old crust side with maximum relief of ~520 m (5)	Absent to moderate with localized strong reflection (6)	—	Sub-Moho reflection is imaged within the pseudofault (6)	—
			85–09	1985	40°	47.2°N, 128.3°W	Basement steps down from young crust side to old crust side with maximum relief ~0.3 s (~300 m) (7)	Absent beneath PW, with strong reflections on both sides (7)	Dominantly southwestward dipping reflections are present in a 5-km wide zone in the middle and lower crust (7)	The sub-Moho reflective zone originate from the young crust side and extends ~40 km laterally to the old crust side. The reflections extend ~0.5-s TWTT (~1.8 km) beneath Moho (7 and 8)	—
	PA	Inner	34–32	2002	90°	47.2°N, 130.4°W	Topography low with maximum relief of 320 m (5)	Absent to weak (6)	Absent (5)	Absent (6)	—
			35–37-31	2002	90°	47.1°N, 130.6°W	Topography low with maximum relief of 310 m (5)	Absent (6)	—	Absent (6)	—
6	JdF	Inner	34–32	2002	90°	46.4°N, 127.9°W	Topography low with maximum relief of 650 m (5)	Absent to moderate (6)	Absent (5)	Absent (6)	—
			35-37-31	2002	90°	46.3°N, 127.9°W	Topography low with maximum relief of 360 m (5)	Absent to moderate (6)	—	Sub-Moho reflection is imaged within the pseudofault (6)	—
7	JdF	Outer	85–07	1985	40°	48.3°N, 127.6°W	Basement steps down from young crust side to old crust side with maximum relief ~0.35 s TWTT (~350 m). Basement topography is rough (8 and 9)	Absent (difficult to determine) (8 and 9)	Dipping, subhorizontal, and lenticular reflections are present in the middle and lower crust (8 and 9)	Dipping and subhorizontal reflections extending to ~1 s beneath the projected Moho level with lateral extent: ~18 km (8 and 9)	Reduced Vp of 7.2 km/s at a depth of 11 km below basement (10)
	a		85–09	1985	30°–40°		Topographic high of relief 0.3-s TWTT (~300–380 m) (8 and 9)	Strong (8 and 9)	Absent (8 and 9)	Dipping and lenticular feature are present at young crust side beneath Moho, with lateral extent ~ 5 km and thickness 1.5–1.8 km (8 and 9)	—

Note. References: (1) Han et al. (2016); (2) Horning et al. (2016); (3) This study; (4) Canales et al. (2017); (5) Carbotte et al. (2008); (6) Nedimović et al. (2005); (7) Calvert et al. (1990); (8) Hasselgren et al. (1992); (9) Hasselgren and Clowes (1995); (10) McClymont & Clowes (2005). Abbreviations: JdF = Juan de Fuca; TWTT = two-way travel time; wrt = with respect to.
[a]Based on the latest isochron map of Wilson (2002), line 85-09 of Hasselgren et al. (1992), and Hasselgren and Clowes (1995) does not cross PW7.

deformation (Hey et al., 1980), and hence, these regions provide a more sheltered environment in which frozen, subcrustal magma lenses can be preserved (Nedimović et al., 2005).

In summary, active source seismic data show that propagator wakes are heterogeneities in the JdF Plate with distinct basement topography and crustal fabric and are potentially more fractured and hydrated at lower crustal and uppermost mantle levels.

6.1.3. Implications for Plate Interface Slip Behavior

Observations from our experiment and earlier studies of propagator pseudofault zones within the JdF Plate (Table 2 and Figure 7) indicate that these features are important structural and hydration anomalies. These zones may be analogous to fracture zones as local heterogeneities in subducting plates that influence plate interface slip behavior. Canales et al. (2017) note that the landward projection of PW2 and PW3 coincide with the boundaries between paleoearthquake rupture segments inferred from turbidite records (Goldfinger et al., 2017) and propose that an increase in the amount of fluids released from the subducted hydrated pseudofaults may contribute to small-scale plate interface stress heterogeneities that act as rupture barriers.

Further downdip along the slab interface, ETS events along the Cascadia margin show segmentation in recurrence intervals with primary boundaries at 42.8°N and 47.5°N. Within these large segments, smaller segments with similar recurrence intervals but different occurrence timing are also defined (Boyarko et al., 2015; Brudzinski & Allen, 2007). Current interpretations mostly attribute variations in ETS recurrence intervals to differences in composition/permeability of the Wrangellia, Siletzia, and Klamath terranes in the overriding North American Plate (Audet & Bürgmann, 2014; Brudzinski & Allen, 2007). Low tremor density zones have been linked to fluid drainage through upper plate faults (Wells et al., 2017). While some of these faults lie close to the boundaries of ETS segments defined from recurrence interval and occurrence timing, others cross the segment centers.

We observe that the boundaries between ETS Segments 1 and 2 and between Segments 6 and 7 coincide or lie in the vicinity of the projected locations of propagator wakes in the downgoing plate (Figure 1b). ETS Segment 5 correlates well with the broad PW1 beneath central Oregon. Beneath south Vancouver Island and Washington, where slab dip varies and hence larger uncertainties are associated with the projected propagator wake locations (Wilson, 2002), no apparent correlation is observed between ETS segment boundaries and propagator wakes (Figure 1b). Based on these spatial relationships, we suggest that propagator wakes may also play a role in ETS segmentation. With the observed characteristics of propagator wakes (Table 2 and Figure 7), we envision three potential mechanisms by which propagator wakes could induce anomalous mechanical properties and stress state along the plate interface and contribute to ETS segmentation.

1. *Effect of basement topographic anomalies*. Propagator pseudofault zones are associated with basement anomalies of 250–740 m on the otherwise low-relief JdF Plate crust (Table 2 and Figure 7). As all the propagator wakes that are projected to underlie the Cascadia forearc are inner psuedofaults, the basement topographic lows that are usually associated with them may carry more sediment (a few hundreds of meters thick over several tens of kilometers along-strike distance) to greater depth than adjacent zones. Although the incoming sediment sequence at Cascadia is 2–3-km thick, existing seismic data suggest that there are regions, such as offshore Washington and Vancouver Island, with very little sediment subduction (e.g., Davis & Hyndman, 1989; Han et al., 2017). In these regions, the plate interface properties at propagator wakes with abundant underthrust sediments may be significantly different from the adjacent zones where the oceanic crust is in direct contact with the upper plate.

   At the depths where ETS is observed, the plate interface is inferred to be a thick shear zone from seismic reflection imaging (Li et al., 2015; Nedimović et al., 2003). Observations from exhumed subduction fault rock records provide evidence for viscous deformation of the matrix for which sediment is a major contributing component (relatively weak material) and brittle deformation within the rock blocks (relatively strong material; Bebout & Penniston-Dorland, 2016) and suggest that ETS may arise from a combination of frictional and viscous behaviors (Fagereng & den Hartog, 2017; Hayman & Lavier, 2014). This inference is consistent with observations of tremor propagation, which suggests that tremors may result from rupture of a series of small patches of asperities yet the surrounding regions slip aseismically (Ghosh et al., 2012).

   With subduction of a thicker sediment section within propagator wake zones, it is likely that the plate interface in these regions has fewer asperities and is more prone to aseismic sliding, giving rise to low tremor density. The broad PW1 that is projected to underlie central Oregon between 44.5°N and 46°N is likely

associated with a large basement low similar to PW3 observed along OR transect and Profile 87-89-73-89a (Figure 7) and may constitute a weak plate interface region with presence of abundant sediments. This inference is consistent with the low level of tremor activity in this region.

2. *Effect of crustal hydration anomalies*. Velocity models derived from wide-angle reflection and refraction data reveal reduced velocity in the crust, suggesting enhanced fracturing and hydration in propagator wake zones (Canales et al., 2017; Horning et al., 2016). More fluid released from the crust within propagator wakes may contribute to higher pore fluid pressures at the plate interface, further weakening the plate interface and facilitating aseismic sliding in these regions.
3. *Effect of orientation of crustal fabric*. All the propagator wakes projected to underlie the Cascadia forearc are inner pseudofaults, within which the crustal fabric is expected to be oriented at high angles to that of the adjoining crustal segments. On our MARGIN transect, we observe intracrustal reflectivity within the propagator wakes that is absent on the cross-plate lines, supporting this inference. Fluid connectivity within the slab may be linked to the inherited abyssal hill fault system, with individual abyssal hill faults that may extend for the full length of ridge segments as evident near the JdF Ridge at present (Stakes et al., 2006). Therefore, the different orientation of crustal fabric within the propagator wakes may confine the development and transmission of pore pressure within crustal segments, which is crucial for the occurrence of ETS (Peacock et al., 2011).

In summary, while upper plate structure or composition may contribute to different recurrence intervals of ETS events, as proposed by previous studies (Audet & Bürgmann, 2014; Brudzinski & Allen, 2007; Wells et al., 2017), propagator wakes as structural and hydration heterogeneities in the downgoing plate could induce localized anomalies of plate interface properties and serve as aseismic slip zones compartmenting slow slip and impeding its propagation.

6.2. Transition of Faulting Pattern in the Oceanic Crust Across 45.8°N and Implication for JdF Plate Hydration

In addition to the inherited crustal segmentation defined by propagator wakes, our data indicate a significant boundary in crustal reflectivity near 45.8°N (Figure 2). South of this boundary, the crust as imaged by the MARGIN transect is more reflective with southward and northward dipping events that transect the crust, whereas north of this boundary, the dipping reflections are mostly observed in the upper-to-middle crust and dominantly dip to the north. From images of the OR and WA transects, Han et al. (2016) observe conjugate deep-cutting faults attributed to subduction bending offshore central Oregon and seaward dipping faults confined to the upper- and middle-crust offshore Washington. The dip angles and dip directions of the reflections as well as the regional differences in their depth extent through the crust observed on the MARGIN transect (Figure 2) are consistent with the previously reported differences in subduction bend faulting found on the OR and WA transects. While the earlier study provided no constraints on the along-margin spatial extent of these differences, or where the transition in faulting style occurs, observations from the MARGIN transect indicate that the more intense and more extensive subduction bend-faulting observed offshore central Oregon extends north to 45.8°N.

At this same location, the tomographic velocity models derived from the coincident OBS data (Canales et al., 2017) reveal a reduction in the Vp of the lower crust from north to south consistent with our finding of greater bend faulting to the south. Average Vp in the lower crust changes from 7.1 km/s north of 45.8°N to 6.9 km/s south of 45.5°N, which can be explained by enhanced porosity and alteration due to more extensive and through-crust faulting offshore Oregon. Further supporting evidence comes from observations of the distribution of seismicity in the JdF Plate. Very few earthquakes are detected in the JdF Plate near the deformation front north of 46°N by the regional land-based catalogs (the Pacific Northwest Seismic Network, the Northern California Seismic Network, and the Canadian National Seismograph Network) and Cascadia Initiative OBS array, whereas abundant seismicity in the incoming JdF Plate near the deformation front is recorded south of this boundary, indicating more active deformation to the south (Figure 1; Canales et al., 2017; Stone et al., 2018). Based on fault geometry and fault throw variation from the JdF Ridge-to-Trench data (Han et al., 2016), the maximum magnitudes of outer-rise earthquakes offshore Washington and Oregon are estimated to be *Mw* 4.0–5.0 and *Mw* 5.3–5.9, respectively (supporting information). This estimate assumes that the bending-related elastic energy stored in the oceanic plate during one megathrust earthquake cycle is released in one major outer-rise earthquake following a megathrust earthquake. This assumption may be

unlikely as the bending-related elastic energy may be released by many smaller outer-rise earthquakes distributed throughout the megathrust earthquake cycle. Therefore, our estimation represents the high end of the outer-rise earthquake magnitude in this region. The subduction bending faults imaged are associated with minimal offset at seafloor, close to or below the resolution of our seismic data (3–5 m), suggesting relatively small tsunami hazards associated with these faults.

It is noteworthy that 45.8°N–46°N is not at an inherited segment boundary within the JdF Plate structure defined by the propagator wakes. Intriguingly, a number of changes in Cascadia subduction zone structure and processes also occur near this latitude (Figure 1). The strike of the deformation front and that of the thrust ridges in the accretionary wedge change from N-S to NNW-SSE near 45.8°N. With the change in strike of ~15°, subduction transitions from ~30° oblique to the margin south of 46°N to closer to orthogonal to the margin further north. With an arch in the downgoing plate centered beneath the Olympic Peninsula (McCrory et al., 2012) attributed to the changing orientation of the subduction zone (Chiao & Creager, 2002), the dip of the plate changes along the margin near 46°N with shallower dips beneath Washington (Figure 1). In the upper plate, the basaltic Siletz terrane extends offshore between 43°N and 46°N (Fleming & Trehu, 1999; McCrory & Wilson, 2013; Tréhu et al., 1994). Within the same latitude range, some models of land-based geodetic data indicate reduced locking of the plate interface in this region compared with further to the north and south (Burgette et al., 2009; McCaffrey et al., 2013; Schmalzle et al., 2014). Although the ability of land-based observations to resolve along-strike variations in current plate interface locking offshore is limited, it is noteworthy that changes at 46°N and 43°N are also evident in observations of plate interface slip distribution from past earthquakes (Goldfinger et al., 2017; P. Wang et al., 2013; K. Wang & Tréhu, 2016; Figure 1).

This suite of coincident changes in plate and subduction zone properties near 46°N is intriguing and warrants further exploration. Our observation of different extents of crustal deformation in the JdF Plate near the deformation front to the south compared to north of 46°N indicates along-strike variations in intraplate stress. With the larger curvature of the JdF Plate near the deformation front and beneath the forearc south of 46°N (Han et al., 2016; McCrory et al., 2012), greater bending stress offshore Oregon is expected. Furthermore, with the change in the strike of the deformation front near 45.8°N, oblique subduction of the JdF Plate south of this boundary should generate a margin-parallel component of subduction resistance. This resistance, along with ridge push and push from the Pacific Plate across the Blanco and Mendocino transform faults, results in a predicted NE-SW compressive stress in the JdF Plate south of 46°N (K. Wang et al., 1997). We speculate that the predicted larger differential stress within the JdF Plate south of 46°N combined with inherited crustal fabric that is subparallel to the trench and thus of optimal orientation for reactivation of abyssal hill faults due to plate bending (Han et al., 2016), leads to more extensive faulting deformation and associated plate hydration offshore Oregon.

6.3. Oblique SSFs at Cascadia Margin

The oblique SSFs found near the deformation front and beneath the continental slope along the Cascadia margin have been proposed to accommodate much of the oblique portion of plate convergence in this region through rotation of upper plate blocks and shortening of the forearc and may affect the generation of megathrust earthquakes along the margin (Goldfinger et al., 1992). Yet mechanisms governing the formation of these faults are not well understood. To address the question of the origin of these oblique SSFs, it is important to understand whether the strike-slip deformation involves the oceanic crust of the JdF Plate or not. Previous seismic studies conducted in the 1980s and 1990s showed that the Alvin Canyon, Daisy Bank, and Wecoma Faults are associated with offsets in the oceanic basement but were unable to discriminate between throughgoing rupture of the oceanic crust or a more superficial detachment of the upper crust (Goldfinger et al., 1997). As the airgun source used in these prior studies was not powerful enough to image basement near the North and South Nitinat Faults, whether these two faults offset the oceanic basement remained unresolved (Goldfinger et al., 1997). Our MARGIN transect crosses four of the five major SSFs at a distance of 11–16 km seaward of the deformation front. The southernmost Alvin Canyon Fault has a similar net slip on the JdF Plate (2.2 ± 0.5 km) and a similar age (380 ± 50 ka) as the nearby Daisy Bank Fault, yet its trace on the seafloor only extends to 7 km seaward of the deformation front, and its vertical offset is less than that of the other SSFs, which may account for it not being detected on our MARGIN line. From the new MCS images, we observe that the two SSFs offshore Washington are associated with basement offsets, similar to

those offshore Oregon (Figures 4f and 4g). Furthermore, our images resolve the base of the oceanic crust and reveal a step in Moho reflection beneath the North Nitinat Fault and an abrupt change in Moho reflection amplitude beneath and near the Daisy Bank and South Nitinat Faults (Figures 4a and 4e), indicating that these SSFs extend through the entire oceanic crust. As the shear strength of intact oceanic crust is much larger than that of the plate interface zone (K. Wang et al., 1995), it would be difficult for a SSF that originated in the upper plate to propagate downward into the JdF Plate and rupture the 6-km-thick oceanic crust. We conclude that these SSFs originate from the oceanic plate.

Besides the four prominent SSFs, our images also reveal a number of steeply dipping faults (with apparent dips of 60°–80°) in the sediment section, evident as coherent offsets in the sediment layers, many of which are connected to offsets in the top of the oceanic crust. The origin of these small faults is unclear. These faults are unlikely to coincide with the subduction bending normal faults imaged near the deformation front (Han et al., 2016) as the observed dips of 60°–80° are too steep (predicted dips for normal faults oriented subparallel to the margin are 20°–30°, see section 5). Indeed, we expect that the subduction bending normal faults observed on the OR and WA transects would be very difficult to recognize in the sediment section on the MARGIN transect. These faults are growth faults with offsets generally decreasing upward from the basement. Variation of fault offset along strike and curvature of fault planes are also common. With these complications, the expected traces of these normal faults along the MARGIN transect would be curved lines at low angle with the sediment stratigraphy, with varying (and unidentifiable in places) offsets. Without direct constraints from dip lines, these low-angle disruptions of sediment layers would be difficult to confidently differentiate from irregular layering within the sediment section.

What then is the origin of the small steeply dipping faults? The association of these faults with basement offsets suggests that they also involve the crust. Without constraints from crossing lines, we cannot determine the strike and true dip of these faults. However, as the true dip must be larger than or equal to the apparent dip, many of these faults may be even steeper than imaged. One possibility is that these faults are small SSFs, perhaps younger and presumably with less accumulated strain than the five prominent ones, and that they form in response to the same regional intraplate stress environment as the larger faults. Goldfinger et al. (1997) propose that the shear couple resulting from viscous mantle resistance to the oblique motion of the slab is responsible for transverse rupture along the major SSFs. The numerical modeling of K. Wang et al. (1997) indicates that oblique subduction south of 46°N causes a margin-parallel component of subduction resistance. This force, along with transform push and ridge push, results in compressive stress in the NE-SW direction and tensile stress in the NW-SE direction, which may facilitate strike-slip deformation. From our MARGIN line, we observe more abundant small steeply dipping faults south of 46°N than further north (Figure 2), with slightly larger offsets (Figure 6d), which is consistent with more deformation south of 46°N. There is no evidence for these small steeply dipping faults along the OR and WA transects. However, if the strike of these faults is parallel to the trend of the major SSFs, they would be subparallel to the two cross-margin lines, and therefore unlikely to be detected.

It is noteworthy that along the MARGIN transect, the large-offset faults (>50 m) are present near the propagator wakes within distances of 25–75 and 260–300 km (Figure 6), whereas faults in the middle of the crustal segments are associated with smaller offsets of 10–30 m. As the sheared and rotated crust within these propagator wakes is weaker than normal crust, strike-slip deformation may tend to focus in these weak zones and further develop into the major SSFs that rupture the crust and have the largest offset.

We speculate that the major and minor SSFs in the JdF Plate play an important role in accommodating intraplate deformation in this region and may contribute to the higher intraplate seismicity south of 46°N (Canales et al., 2017; Stone et al., 2018).

7. Conclusions

Through PSTM imaging of MCS data acquired along the Cascadia margin, we characterize the along-strike variation of the sediment section, oceanic crust, and uppermost mantle of the JdF Plate from 44.3°N to 47.8°N just prior to subduction. Our major findings and conclusions are the following:

1. Propagator wakes are typically associated with basement topographic anomalies, absent/weak Moho reflections, and orientation-dependent crustal reflectivity, indicating that they are heterogeneities with distinct crustal fabrics and are more fractured and hydrated than the surrounding oceanic crust.

Beneath the Cascadia forearc, the boundaries of some of the paleoearthquake rupture segments and ETS events lie in the vicinity of the propagator wakes in the downgoing plate. We propose that the anomalies in basement topography, crustal fabric, and hydration state associated with the propagator wakes could induce anomalous mechanical properties and stress state along the plate interface and contribute to ETS segmentation.

2. Our MCS images reveal abundant crustal reflectivity along the margin and a change around 45.8°N from predominantly antithetic reflections that extend through the lower crust to synthetic north facing reflections confined mostly to the middle-to-upper crust. The apparent dips of these reflections and their depth distribution in the crust are consistent with the dips and depth distribution of normal faults imaged on the two cross-plate transects within ~40 km seaward of the deformation front attributed to subduction bend faulting. The change in crustal reflectivity coincides with a reduction in lower crustal/upper mantle Vp from north to south across 45.8°N observed from the coincident seismic refraction study (Canales et al., 2017). Together, these observations indicate an increase in the extent of subduction bend faulting south of 45.8°N, which is accompanied by increased hydration compared with an essentially dry lower crust/upper mantle further north. The more extensive faulting deformation south of 45.8°N likely results from along-strike changes in slab dip and resistance to subduction and is linked to changes in the strike of the deformation front across 46°N.
3. The four previously identified WNW trending SSFs crossed by our line transect the entire sediment section and are associated with offsets of the oceanic basement and abrupt changes in depth and/or amplitude of the Moho reflection, indicating that they extend through the entire crust. Our images also reveal a number of steeply dipping faults (with apparent dips of 60°–80°) within the sediment section, which may be additional small SSFs. The observations from our study indicate that these SSFs originate in the subducting JdF Plate as proposed by Goldfinger et al. (1997) and are associated with a complex regional stress field (K. Wang et al., 1997). That the major SSFs are close to the propagator wakes suggests that the weaker crust near these zones may focus strike-slip deformation more effectively.
4. A seamount 15.3-km wide at its base and 1.2 km high above surrounding basement is imaged at 125.69°W, 45.43°N. This seamount may belong to the group of seamounts that have been inferred from sea surface magnetic and gravity data beneath the Cascadia forearc between 44°N and 45°N (Tréhu et al., 2012).

Acknowledgments
We thank the R/V *M.G. Langseth*'s Captain M. Landow, crew, and technical staff led by R. Steinhaus for their efforts, which made possible the success of cruise MGL1211. Seismic data processing and interpretation was conducted using the Paradigm processing software packages Focus, Geodepth, and VoxelGeo. All MCS field data, seismic navigation, and acquisition logs are archived with the IEDA: Marine Geoscience Data System (Carbotte et al., 2012, doi: 10.1594/IEDA/319000). The processed seismic data are archived at Academic Seismic Portal (doi: 10.1594/IEDA/500069). We thank Tom Brocher and an anonymous reviewer for insightful comments and suggestions that helped us improve the paper. This research was supported by NSF grant OCE 1029411 to S. M. C., H. C., and M. R. N. and 1029305 to J. P. C.

References

Appelgate, B., Goldfinger, C., Mackay, M. E., Kulm, L. D., Fox, C. G., Embley, R. W., & Meis, P. J. (1992). A left-lateral strike-slip-fault seaward of the Oregon convergent margin. *Tectonics*, *11*(3), 465–477. https://doi.org/10.1029/91TC02906

Atwater, B. F. (1987). Evidence for great Holocene earthquakes along the outer coast of Washington-state. *Science*, *236*(4804), 942–944. https://doi.org/10.1126/science.236.4804.942

Atwater, B. F., & Hemphill-Haley, E. (1997). Recurrence intervals for great earthquakes of the past 3,500 years at northeastern Willapa Bay, Washington.

Audet, P., & Bürgmann, R. (2014). Possible control of subduction zone slow-earthquake periodicity by silica enrichment. *Nature*, *510*(7505), 389–392. https://doi.org/10.1038/nature13391

Bebout, G. E., & Penniston-Dorland, S. C. (2016). Fluid and mass transfer at subduction interfaces—The field metamorphic record. *Lithos*, *240*, 228–258.

Bell, R., Sutherland, R., Barker, D. H. N., Henrys, S., Bannister, S., Wallace, L., & Beavan, J. (2010). Seismic reflection character of the Hikurangi subduction interface, New Zealand, in the region of repeated Gisborne slow slip events. *Geophysical Journal International*, *180*(1), 34–48. https://doi.org/10.1111/j.1365-246X.2009.04401.x

Boulahanis, B., Carbotte, S. M., Huybers, P. J., Langmuir, C. H., Han, S., Aghaei, O., et al. (2015). Mid-ocean ridge magma supply and glacial cycles: Long time series studies of crustal thickness and seafloor topography, *AGU Fall Meeting Abstract*.

Boyarko, D. C., Brudzinski, M. R., Porritt, R. W., Allen, R. M., & Tréhu, A. M. (2015). Automated detection and location of tectonic tremor along the entire Cascadia margin from 2005 to 2011. *Earth and Planetary Science Letters*, *430*, 160–170.

Brocher, T. M., Wells, R. E., Lamb, A. P., & Weaver, C. S. (2017). Evidence for distributed clockwise rotation of the crust in the northwestern United States from fault geometries and focal mechanisms. *Tectonics*, *36*, 787–818. https://doi.org/10.1002/2016TC004223

Brudzinski, M. R., & Allen, R. M. (2007). Segmentation in episodic tremor and slip all along Cascadia. *Geology*, *35*(10), 907–910. https://doi.org/10.1130/g23740a.1

Burgette, R. J., Weldon, R. J., & Schmidt, D. A. (2009). Interseismic uplift rates for western Oregon and along-strike variation in locking on the Cascadia subduction zone. *Journal of Geophysical Research*, *114*, B01408. https://doi.org/10.1029/2008JB005679

Calvert, A. J. (1995). Seismic evidence for a magma chamber beneath the slow-spreading Mid-Atlantic Ridge. *Nature*, *377*(6548), 410–414. https://doi.org/10.1038/377410a0

Calvert, A. J., Hasselgren, E. A., & Clowes, R. M. (1990). Oceanic rift propagation—A cause of crustal underplating, and seamount volcanism. *Geology*, *18*(9), 886–889. https://doi.org/10.1130/0091-7613(1990)018%3C0886:ORPACO%3E2.3.CO;2

Canales, J. P., Carbotte, S. M., Nedimović, M. R., & Carton, H. (2017). Dry Juan de Fuca slab revealed by quantification of water entering Cascadia subduction zone. *Nature Geoscience*, *10*(11), 864–870. https://doi.org/10.1038/ngeo3050

Canales, J. P., Detrick, R. S., Carbotte, S. M., Kent, G. M., Diebold, J. B., Harding, A., et al. (2005). Upper crustal structure and axial topography at intermediate spreading ridges: Seismic constraints from the southern Juan de Fuca Ridge. *Journal of Geophysical Research*, *110*, B12104. https://doi.org/10.1029/2005JB003630

Carbotte, S. M., Canales, J. P., Carton, H., & Nedimović, M. R. (2012). Multi-channel seismic shot data from the Cascadia subduction zone acquired during the R/V *Marcus G.* Langseth Expedition MGL1211, *Integrated Earth Data Applications (IEDA)*. https://doi.org/10.1594/IEDA/319000

Carbotte, S. M., Nedimovic, M. R., Canales, J. P., Kent, G. M., Harding, A. J., & Marjanovic, M. (2008). Variable crustal structure along the Juan de Fuca Ridge: Influence of on-axis hot spots and absolute plate motions. *Geochemistry, Geophysics, Geosystems*, *9*, Q08001. https://doi.org/10.1029/2007GC001922

Chiao, L.-Y., & Creager, K. C. (2002). Geometry and membrane deformation rate of the subducting Cascadia slab, *The Cascadia subduction zone and related subduction system—Seismic structure, intraslab earthquakes and processes, and earthquake hazards*, 02–328.

Choo, J., Downton, J., & Dewar, J. (2004). Lift: A new and practical approach to noise and multiple attenuation. *First Break*, *22*(5), 39–44.

Contreras-Reyes, E., & Carrizo, D. (2011). Control of high oceanic features and subduction channel on earthquake ruptures along the Chile–Peru subduction zone. *Physics of the Earth and Planetary Interiors*, *186*(1-2), 49–58. https://doi.org/10.1016/j.pepi.2011.03.002

Davis, E. E., & Hyndman, R. D. (1989). Accretion and recent deformation of sediments along the northern Cascadia subduction zone. *Geological Society of America Bulletin*, *101*(11), 1465–1480. https://doi.org/10.1130/0016-7606(1989)101%3C1465:AARDOS%3E2.3.CO;2

Fagereng, Å., & den Hartog, S. A. M. (2017). Subduction megathrust creep governed by pressure solution and frictional-viscous flow. *Nature Geoscience*, *10*(1), 51–57. https://doi.org/10.1038/ngeo2857

Fleming, S. W., & Trehu, A. M. (1999). Crustal structure beneath the central Oregon convergent margin from potential-field modeling: Evidence for a buried basement ridge in local contact with a seaward dipping backstop. *Journal of Geophysical Research*, *104*(B9), 20,431–20,447. https://doi.org/10.1029/1999JB900159

Ghosh, A., Vidale, J. E., & Creager, K. C. (2012). Tremor asperities in the transition zone control evolution of slow earthquakes. *Journal of Geophysical Research*, *117*, B10301. https://doi.org/10.1029/2012JB009249

Goldfinger, C., Galer, S., Beeson, J., Hamilton, T., Black, B., Romsos, C., et al. (2017). The importance of site selection, sediment supply, and hydrodynamics: A case study of submarine paleoseismology on the northern Cascadia margin, Washington USA. *Marine Geology*, *384*, 4–46. https://doi.org/10.1016/j.margeo.2016.06.008

Goldfinger, C., Kulm, L. D., Yeats, R. S., Appelgate, B., Mackay, M. E., & Cochrane, G. R. (1996). Active strike-slip faulting and folding of the Cascadia plate boundary and forearc in central and northern Oregon, *Assessing and reducing earthquake hazards in the Pacific Northwest, USGS Professional Paper 1560*, *1*.

Goldfinger, C., Kulm, L. D., Yeats, R. S., Appelgate, B., Mackay, M. E., & Moore, G. F. (1992). Transverse structural trends along the Oregon convergent margin—Implications for Cascadia earthquake potential and crustal rotations. *Geology*, *20*(2), 141–144. https://doi.org/10.1130/0091-7613(1992)020%3C0141:tstato%3E2.3.co;2

Goldfinger, C., Kulm, L. D., Yeats, R. S., Hummon, C., Huftile, G. J., Niem, A. R., & McNeill, L. C. (1996). Oblique strike-slip faulting of the Cascadia submarine forearc: The Daisy Bank fault zone off central Oregon. In *Subduction top to bottom* (pp. 65–74). Washington, DC: American Geophysical Union.

Goldfinger, C., Kulm, L. D., Yeats, R. S., McNeill, L., & Hummon, C. (1997). Oblique strike-slip faulting of the Central Cascadia submarine forearc. *Journal of Geophysical Research*, *102*(B4), 8217–8243. https://doi.org/10.1029/96JB02655

Goldfinger, C., Nelson, C. H., & Johnson, J. E. (2003). Holocene earthquake records from the Cascadia subduction zone and northern San Andreas fault based on precise dating of offshore turbidites. *Annual Review of Earth and Planetary Sciences*, *31*(1), 555–577. https://doi.org/10.1146/annurev.earth.31.100901.141246

Han, S., Bangs, N. L., Carbotte, S. M., Saffer, D. M., & Gibson, J. C. (2017). Links between sediment consolidation and Cascadia megathrust slip behaviour. *Nature Geoscience*, *10*(12), 954–959. https://doi.org/10.1038/s41561-017-0007-2

Han, S., Carbotte, S. M., Canales, J. P., Nedimović, M. R., Carton, H., Gibson, J. C., & Horning, G. W. (2016). Seismic reflection imaging of the Juan de Fuca plate from ridge to trench: New constraints on the distribution of faulting and evolution of the crust prior to subduction. *Journal of Geophysical Research*, *121*, 1849–1872. https://doi.org/10.1002/2015JB012416

Hasselgren, E., & Clowes, R. M. (1995). Crustal structure of northern Juan de Fuca Plate from multichannel reflection data. *Journal of Geophysical Research*, *100*(B4), 6469–6486. https://doi.org/10.1029/94JB02941

Hasselgren, E., Clowes, R. M., & Calvert, A. J. (1992). Propagating rift pseudofaults—Zones of crustal underplating imaged by multichannel seismic reflection data. *Geophysical Research Letters*, *19*(5), 485–488. https://doi.org/10.1029/92GL00368

Hayman, N. W., & Lavier, L. L. (2014). The geologic record of deep episodic tremor and slip. *Geology*, *42*(3), 195–198. https://doi.org/10.1130/G34990.1

Henstock, T. J., McNeill, L. C., Bull, J. M., Cook, B. J., Gulick, S. P. S., Austin, J. A., et al. (2016). Downgoing plate topography stopped rupture in the AD 2005 Sumatra earthquake. *Geology*, *44*(1), 71–74. https://doi.org/10.1130/G37258.1

Hey, R. N., Duennebier, F. K., & Morgan, W. J. (1980). Propagating rifts on midocean ridges. *Journal of Geophysical Research*, *85*(NB7), 3647–3658. https://doi.org/10.1029/JB085iB07p03647

Horning, G., Canales, J. P., Carbotte, S. M., Han, S., Carton, H., Nedimović, M. R., & Keken, P. E. (2016). A 2-D tomographic model of the Juan de Fuca plate from accretion at axial seamount to subduction at the Cascadia margin from an active source ocean bottom seismometer survey. *Journal of Geophysical Research*, *121*, 5859–5879. https://doi.org/10.1002/2016JB013228

Jones, D. L., Silberling, N. J., & Hillhouse, J. (1977). Wrangellia—A displaced terrane in northwestern North America. *Canadian Journal of Earth Sciences*, *14*(11), 2565–2577. https://doi.org/10.1139/e77-222

Karsten, J. L., & Delaney, J. R. (1989). Hot spot-ridge crest convergence in the northeast Pacific. *Journal of Geophysical Research*, *94*(B1), 700–712. https://doi.org/10.1029/JB094iB01p00700

Kent, G. M., Kim, I. I., Harding, A. J., Detrick, R. S., & Orcutt, J. A. (1996). Suppression of sea-floor scattered energy using a dip moveout approach—Application to the mid-ocean ridge environment. *Geophysics*, *61*(3), 821–834. https://doi.org/10.1190/1.1444007

Kirby, S., Engdahl, R. E., & Denlinger, R. (1996). Intermediate-depth intraslab earthquakes and arc volcanism as physical expressions of crustal and uppermost mantle metamorphism in subducting slabs. In *Subduction top to bottom* (pp. 195–214).

Kleinrock, M. C., & Hey, R. N. (1989). Detailed tectonics near the tip of the Galapagos 95.5 W propagator: How the lithosphere tears and a spreading axis develops. *Journal of Geophysical Research*, *94*(B10), 13,801–13,838.

Kreemer, C., Blewitt, G., & Klein, E. C. (2014). A geodetic plate motion and global strain rate model. *Geochemistry, Geophysics, Geosystems*, *15*, 3849–3889. https://doi.org/10.1002/2014GC005407

Li, J., Shillington, D. J., Bécel, A., Nedimović, M. R., Webb, S. C., Saffer, D. M., et al. (2015). Downdip variations in seismic reflection character: Implications for fault structure and seismogenic behavior in the Alaska subduction zone. *Journal of Geophysical Research: Solide Earth*, *120*, 7883–7904. https://doi.org/10.1002/2015JB012338

Marjanović, M., Carbotte, S. M., Nedimovic, M. R., & Canales, J. P. (2011). Gravity and seismic study of crustal structure along the Juan de Fuca Ridge axis and across pseudofaults on the ridge flanks. *Geochemistry, Geophysics, Geosystems*, *12*, Q05008. https://doi.org/10.1029/2010GC003439

Masson, D. G. (1991). Fault patterns at outer trench walls. *Marine Geophysical Researches*, *13*(3), 209–225. https://doi.org/10.1007/bf00369150

McCaffrey, R. (1991). Slip vectors and stretching of the Sumatran fore arc. *Geology*, *19*(9), 881–884. https://doi.org/10.1130/0091-7613(1991)019%3C0881:svasot%3E2.3.co;2

McCaffrey, R., King, R. W., Payne, S. J., & Lancaster, M. (2013). Active tectonics of northwestern US inferred from GPS-derived surface velocities. *Journal of Geophysical Research: Solid Earth*, *118*, 709–723. https://doi.org/10.1029/2012JB009473

McClymont, A. F., & Clowes, R. M. (2005). Anomalous lithospheric structure of northern Juan de Fuca plate—A consequence of oceanic rift propagation? *Tectonophysics*, *406*(3-4), 213–231. https://doi.org/10.1016/j.tecto.2005.05.026

McCrory, P. A., Blair, J. L., Waldhauser, F., & Oppenheimer, D. H. (2012). Juan de Fuca slab geometry and its relation to Wadati-Benioff zone seismicity. *Journal of Geophysical Research*, *117*, B09306. https://doi.org/10.1029/2012JB009407

McCrory, P. A., & Wilson, D. S. (2013). A kinematic model for the formation of the Siletz-Crescent forearc terrane by capture of coherent fragments of the Farallon and Resurrection plates. *Tectonics*, *32*, 718–736. https://doi.org/10.1002/tect.20045

Métois, M., Socquet, A., & Vigny, C. (2012). Interseismic coupling, segmentation and mechanical behavior of the Central Chile subduction zone. *Journal of Geophysical Research*, *117*, B03406. https://doi.org/10.1029/2011JB008736

Morton, E. A., & Bilek, S. L. (2015). Preliminary event detection of earthquakes using the Cascadia initiative data. *Seismological Research Letters*, *86*(5), 1270–1277. https://doi.org/10.1785/0220150098

Nedimović, M. R., Bohnenstiehl, D. R., Carbotte, S. M., Canales, J. P., & Dziak, R. P. (2009). Faulting and hydration of the Juan de Fuca plate system. *Earth and Planetary Science Letters*, *284*(1–2), 94–102. https://doi.org/10.1016/j.epsl.2009.04.013

Nedimović, M. R., Carbotte, S. M., Harding, A. J., Detrick, R. S., Canales, J. P., Diebold, J. B., et al. (2005). Frozen magma lenses below the oceanic crust. *Nature*, *436*(7054), 1149–1152. https://doi.org/10.1038/nature03944

Nedimović, M. R., Hyndman, R. D., Ramachandran, K., & Spence, G. D. (2003). Reflection signature of seismic and aseismic slip on the northern Cascadia subduction interface. *Nature*, *424*(6947), 416–420. https://doi.org/10.1038/nature01840

Noda, H., & Lapusta, N. (2013). Stable creeping fault segments can become destructive as a result of dynamic weakening. *Nature*, *493*(7433), 518–521. https://doi.org/10.1038/nature11703

Obana, K., Scherwath, M., Yamamoto, Y., Kodaira, S., Wang, K., Spence, G., et al. (2015). Earthquake activity in northern Cascadia subduction zone off Vancouver Island revealed by ocean-bottom seismograph observations. *Bulletin of the Seismological Society of America*, *105*(1), 489–495. https://doi.org/10.1785/0120140095

Peacock, S. M., Christensen, N. I., Bostock, M. G., & Audet, P. (2011). High pore pressures and porosity at 35 km depth in the Cascadia subduction zone. *Geology*, *39*(5), 471–474. https://doi.org/10.1130/g31649.1

Ranero, C. R., Morgan, J. P., McIntosh, K., & Reichert, C. (2003). Bending-related faulting and mantle serpentinization at the Middle America trench. *Nature*, *425*(6956), 367–373. https://doi.org/10.1038/nature01961

Ranero, C. R., Reston, T. J., Belykh, I., & Gnibidenko, H. (1997). Reflective oceanic crust formed at a fast-spreading center in the Pacific. *Geology*, *25*(6), 499–502. https://doi.org/10.1130/0091-7613(1997)025%3C0499:ROCFAA%3E2.3.CO;2

Ranero, C. R., Villaseñor, A., Phipps Morgan, J., & Weinrebe, W. (2005). Relationship between bend-faulting at trenches and intermediate-depth seismicity. *Geochemistry, Geophysics, Geosystems*, *6*, Q12002. https://doi.org/10.1029/2005GC000997

Reston, T. J., Ranero, C. R., & Belykh, I. (1999). The structure of Cretaceous oceanic crust of the NW Pacific: Constraints on processes at fast spreading centers. *Journal of Geophysical Research*, *104*(B1), 629–644. https://doi.org/10.1029/98JB02640

Ryan, W. B. F., Carbotte, S. M., Coplan, J. O., O'Hara, S., Melkonian, A., Arko, R., et al. (2009). Global multi-resolution topography synthesis. *Geochemistry, Geophysics, Geosystems*, *10*, Q03014. https://doi.org/10.1029/2008GC002332

Schmalzle, G. M., McCaffrey, R., & Creager, K. C. (2014). Central Cascadia subduction zone creep. *Geochemistry, Geophysics, Geosystems*, *15*, 1515–1532. https://doi.org/10.1002/2013gc005172

Scott, R., & Henstock, T. (2016). Origin of lower crustal reflectors found in mature fast-spreading crust in the eastern Pacific, *AGU Fall Meeting Abstract*.

Shillington, D. J., Bécel, A., Nedimovic, M. R., Kuehn, H., Webb, S. C., Abers, G. A., et al. (2015). Link between plate fabric, hydration and subduction zone seismicity in Alaska. *Nature Geoscience*, *8*(12), 961–964. https://doi.org/10.1038/ngeo2586

Singh, S. C., Hananto, N., Mukti, M., Robinson, D. P., Das, S., Chauhan, A., et al. (2011). Aseismic zone and earthquake segmentation associated with a deep subducted seamount in Sumatra. *Nature Geoscience*, *4*(5), 308–311. https://doi.org/10.1038/ngeo1119

Stakes, D. S., Perfit, M. R., Tivey, M. A., Caress, D. W., Ramirez, T. M., & Maher, N. (2006). The Cleft revealed: Geologic, magnetic, and morphologic evidence for construction of upper oceanic crust along the southern Juan de Fuca Ridge. *Geochemistry, Geophysics, Geosystems*, *7*, Q04003. https://doi.org/10.1029/2005GC001038

Stone, I., Vidale, J., Han, S., & Roland, E. (2018). Catalog of near-shore seismicity in Cascadia: Insights into the regional distribution of microseismicity and its relation to subduction processes. *Journal of Geophysical Research: Solid Earth*, *123*, 641–652. https://doi.org/10.1002/2017JB014966

Tréhu, A. M., Asudeh, I., Brocher, T. M., Luetgert, J. H., Mooney, W. D., Nabelek, J. L., & Nakamura, Y. (1994). Crustal architecture of the Cascadia fore-arc. *Science*, *266*(5183), 237–243. https://doi.org/10.1126/science.266.5183.237

Tréhu, A. M., Blakely, R. J., & Williams, M. C. (2012). Subducted seamounts and recent earthquakes beneath the Central Cascadia forearc. *Geology*, *40*(2), 103–106. https://doi.org/10.1130/g32460.1

Tréhu, A. M., Braunmiller, J., & Davis, E. (2015). Seismicity of the Central Cascadia continental margin near 44.5°N: A decadal view. *Seismological Research Letters*, *86*(3), 819–829. https://doi.org/10.1785/0220140207

Tréhu, A. M., Braunmiller, J., & Nabelek, J. L. (2008). Probable low-angle thrust earthquakes on the Juan de Fuca-North America plate boundary. *Geology*, *36*(2), 127–130. https://doi.org/10.1130/g24145a.1

Tsutsumi, H., & Okada, A. (1996). Segmentation and Holocene surface faulting on the Median Tectonic Line, southwest Japan. *Journal of Geophysical Research*, *101*(B3), 5855–5871. https://doi.org/10.1029/95JB01913

Wang, K., & Bilek, S. L. (2011). Do subducting seamounts generate or stop large earthquakes? *Geology*, *39*(9), 819–822. https://doi.org/10.1130/g31856.1

Wang, K., He, J. H., & Davis, E. (1997). Transform push, oblique subduction resistance, and intraplate stress of the Juan de Fuca plate. *Journal of Geophysical Research*, *102*(B1), 661–674. https://doi.org/10.1029/96JB03114

Wang, K., Mulder, T., Rogers, G. C., & Hyndman, R. D. (1995). Case for very-low coupling stress on the Cascadia subduction fault. *Journal of Geophysical Research*, *100*(B7), 12,907–12,918. https://doi.org/10.1029/95JB00516

Wang, K., & Tréhu, A. M. (2016). Invited review paper: Some outstanding issues in the study of great megathrust earthquakes—The Cascadia example. *Journal of Geodynamics*, *98*, 1–18. https://doi.org/10.1016/j.jog.2016.03.010

Wang, P., Engelhart, S. E., Wang, K., Hawkes, A. D., Horton, B. P., Nelson, A. R., & Witter, R. C. (2013). Heterogeneous rupture in the great Cascadia earthquake of 1700 inferred from coastal subsidence estimates. *Journal of Geophysical Research: Solid Earth*, *118*, 2460–2473. https://doi.org/10.1002/jgrb.50101

Wells, R. E., Blakely, R. J., Sugiyama, Y., Scholl, D. W., & Dinterman, P. A. (2003). Basin-centered asperities in great subduction zone earthquakes: A link between slip, subsidence, and subduction erosion? art. no. 2507. *Journal of Geophysical Research*, *108*(B10), 2507. https://doi.org/10.1029/2002JB002072

Wells, R. E., Blakely, R. J., Wech, A. G., McCrory, P. A., & Michael, A. (2017). Cascadia subduction tremor muted by crustal faults. *Geology*, *45*(6), 515–518. https://doi.org/10.1130/G38835.1

Wilson, D. S. (1988). Tectonic history of the Fuan de Fuca Ridge over the last 40 million years. *Journal of Geophysical Research*, *93*(B10), 11,863–11,876. https://doi.org/10.1029/JB093iB10p11863

Wilson, D. S. (1993). Confidence-intervals for motion and deformation of the Juan de Fuca Plate. *Journal of Geophysical Research*, *98*(B9), 16,053–16,071. https://doi.org/10.1029/93JB01227

Wilson, D. S. (2002). The Juan de Fuca plate and slab: Isochron structure and Cenozoic plate motions. *The Cascadia Subduction Zone and Related Subduction Systems*, *4350*, 9–12.

Wilson, D. S., Hey, R. N., & Nishimura, C. (1984). Propagation as a mechanism of reorientation of the Juan de Fuca Ridge. *Journal of Geophysical Research*, *89*(NB11), 9215–9225. https://doi.org/10.1029/JB089iB11p09215